Gastroenterology 2022;162:223–237

Epithelial X-Box Binding Protein 1 Coordinates Tumor Protein p53-Driven DNA Damage Responses and Suppression of Intestinal Carcinogenesis

Lina Welz,[1,2] Nassim Kakavand,[1] Xiang Hang,[1] Georg Laue,[1] Go Ito,[1,3] Miguel Gomes Silva,[4] Christina Plattner,[5] Neha Mishra,[1] Felicitas Tengen,[6] Christoph Ogris,[6] Moritz Jesinghaus,[7] Felix Wottawa,[1] Philipp Arnold,[8] Leena Kaikkonen,[9] Stefanie Stengel,[1] Florian Tran,[1,2] Saumya Das,[9] Arthur Kaser,[10] Zlatko Trajanoski,[5] Richard Blumberg,[11] Christoph Roecken,[12] Dieter Saur,[4] Markus Tschurtschenthaler,[4] Stefan Schreiber,[1,2] Philip Rosenstiel,[1,§] and Konrad Aden[1,2,§]

[1]Institute of Clinical Molecular Biology, Christian-Albrechts-University and University Hospital Schleswig-Holstein, Campus Kiel, Kiel, Germany; [2]Department of Internal Medicine I, Christian-Albrechts-University and University Hospital Schleswig-Holstein, Campus Kiel, Kiel, Germany; [3]Department of Gastroenterology and Hepatology, Tokyo Medical and Dental University, Tokyo, Japan; [4]Center for Translational Cancer Research (TranslaTUM), Technische Universität München, Munich, Germany; [5]Institute of Bioinformatics, Medical University of Innsbruck, Innsbruck, Austria; [6]Institute of Computational Biology, Helmholtz Zentrum München, Munich, Germany; [7]Institute of Pathology, University Hospital Marburg, Marburg, Germany; [8]Institute of Functional and Clinical Anatomy, Friedrich-Alexander-University Erlangen-Nürnberg (FAU), Erlangen, Germany; [9]Cardiovascular Research Center, Massachusetts General Hospital, Boston, Massachusetts; [10]Division of Gastroenterology and Hepatology, Department of Medicine, Addenbrooke's Hospital, University of Cambridge, Cambridge, United Kingdom; [11]Gastroenterology Division, Department of Medicine, Brigham and Women's Hospital, Harvard Medical School, Boston, Massachusetts; and [12]Department of Pathology, Christian-Albrechts-University and University Hospital Schleswig-Holstein, Campus Kiel, Kiel, Germany

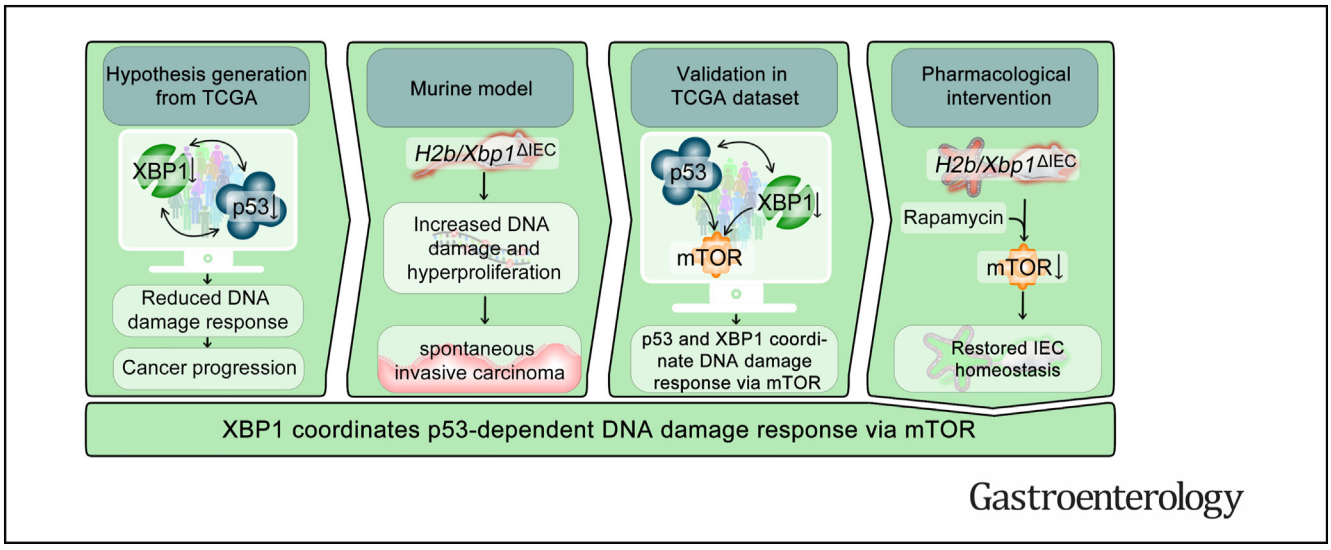

BACKGROUND & AIMS: Throughout life, the intestinal epithelium undergoes constant self-renewal from intestinal stem cells. Together with genotoxic stressors and failing DNA repair, this self-renewal causes susceptibility toward malignant transformation. X-box binding protein 1 (XBP1) is a stress sensor involved in the unfolded protein response (UPR). We hypothesized that XBP1 acts as a signaling hub to regulate epithelial DNA damage responses. **METHODS:** Data from The Cancer Genome Atlas were analyzed for association of XBP1 with colorectal cancer (CRC) survival and molecular interactions between XBP1 and p53 pathway activity. The role of XBP1 in orchestrating p53-driven DNA damage response was tested in vitro in mouse models of chronic intestinal epithelial cell (IEC) DNA damage (*Xbp1/H2b*$^{fl/fl}$, *Xbp1*$^{\Delta IEC}$, *H2b*$^{\Delta IEC}$, *H2b/Xbp1*$^{\Delta IEC}$) and via orthotopic tumor organoid transplantation. Transcriptome analysis of intestinal organoids was performed to identify molecular targets of Xbp1-mediated DNA damage response. **RESULTS:** In The Cancer Genome Atlas data set of CRC, low *XBP1* expression was significantly associated with poor overall survival and reduced p53 pathway activity. In vivo, *H2b/Xbp1*$^{\Delta IEC}$ mice developed spontaneous intestinal carcinomas. Orthotopic tumor organoid transplantation revealed a metastatic potential of *H2b/Xbp1*$^{\Delta IEC}$-derived tumors. RNA sequencing of intestinal organoids (*H2b/Xbp1*$^{fl/fl}$, *H2b*$^{\Delta IEC}$, *H2b/*

Xbp1$^{\Delta IEC}$, and *H2b/p53*$^{\Delta IEC}$) identified a transcriptional program downstream of p53, in which XBP1 directs DNA-damage-inducible transcript 4-like (*Ddit4l*) expression. DDIT4L inhibits mechanistic target of rapamycin-mediated phosphorylation of 4E-binding protein 1. Pharmacologic mechanistic target of rapamycin inhibition suppressed epithelial hyperproliferation via 4E-binding protein 1. **CONCLUSIONS:** Our data suggest a crucial role for XBP1 in coordinating epithelial DNA damage responses and stem cell function via a p53-DDIT4L–dependent feedback mechanism.

Keywords: DNA Damage; XBP1; p53; Intestinal Epithelial Cell; CRC.

X-box binding protein 1 (XBP1) is an endoplasmic reticulum (ER)-resident protein coordinating the unfolded protein response (UPR) via translocation of a spliced *sXBP1* transcript that acts as a nuclear transcription factor.[1] Multiple studies have underlined the role of XBP1 in various cancer types, albeit with contradictory effects on the directionality of the overall outcome. With regard to colorectal cancer (CRC), murine studies investigating the role of XBP1 in intestinal epithelial carcinogenesis point toward a tumor suppressive role of the inositol-requiring enzyme type 1 (IRE1)/XBP1 axis, as epithelial specific deletion of *Xbp1* results in epithelial hyperproliferation and increased tumor burden in experimental cancer models (azoxymethane [AOM]/dextran sodium sulfate [DSS]; *Apc*$^{Min/+}$ mice).[2] Yet, the exact mechanism of this effect and its importance for sporadic CRC, which represents the majority of CRC cases, remains unknown.

In sporadic CRC, genomic instability and impaired DNA repair have been recognized as essential cellular properties that enable the acquisition of mutations in oncogenes or tumor-suppressor genes encoding, for example, phosphatidylinositol-4,5-bisphosphate 3-kinase catalytic subunit alpha (PIK3CA) and tumor protein p53 (TP53), transforming growth factor-β receptors and SMADs, thereby explaining the sequential adenoma to carcinoma transformation.[3] In addition, proto-oncogenes, such as *KRAS*, *BRAF,* and frequent mutations within the Wnt-signaling pathway (*APC*, *CTNNB1*) contribute to the pathogenesis of CRC. Functionally, all of these mutations converge in the activation of the Wnt, Ras/Raf/MEK (mitogen activated protein kinase/ERK kinase)/ERK (extracellular-signal-regulated-kinase), or phosphatidylinositol-3-kinase/AKT pathway.[4,5]

It has been shown that ribonucleotide excision repair (RER) is responsible for removing misincorporated ribonucleotides from replicating DNA, with the ribonuclease H2 (RNaseH2) complex providing the first key step of RER by cleaving 5′ of the DNA-embedded ribonucleotide.[6] Intestinal ablation of RNaseH2, subunit B (*Rnaseh2b*) in murine epithelium (intestinal epithelial cell [IEC]) (*H2b*$^{\Delta IEC}$) results in spontaneous DNA damage associated with proliferative exhaustion of the resident stem cell compartment.[7] Notably, codeletion of the tumor suppressor p53 in *H2b/p53*$^{\Delta IEC}$ mice promoted spontaneous age-dependent formation of intestinal carcinomas.

WHAT YOU NEED TO KNOW

BACKGROUND AND CONTEXT

The inflammatory bowel disease risk gene X-box protein 1 essentially coordinates epithelial cell function and thereby contributes to intestinal mucosal homeostasis. Ribonuclease H2 facilitates ribonucleotide excision repair and loss of epithelial ribonuclease H2 subunit B (*RNASEH2B*) leads to the development of DNA damage. Whether X-box protein 1 is involved in intestinal epithelial DNA damage responses is not yet known.

NEW FINDINGS

Simultaneous deficiency of epithelial X-box protein 1 (*Xbp1*) and *Rnaseh2b* leads to the generation of aggressive metastatic intestinal adenocarcinoma in mice. Mechanistically, *Xbp1* restrains intestinal stem cell proliferation and consecutive carcinogenesis via p53-DNA damage inducible transcript 4-like–mediated mechanistic target of rapamycin inhibition.

LIMITATIONS

The exact molecular mechanism of how X-box protein 1 licences DNA damage responses needs to be elucidated.

IMPACT

This study puts forward a novel concept in which chronic intestinal endothelial reticulum stress and DNA damage converge into a layer of susceptibility for intestinal carcinogenesis.

A limited body of evidence indicates that XBP1 might directly be involved in regulating DNA damage response (DDR) by means of interfering with double-strand break repair or p53-driven DDR.[8–10] In addition, it has been demonstrated that the resolution of genotoxic stress necessitates IRE1α, the upstream protein facilitating XBP1 splicing in response to ER stress, in a mechanism involving regulated IRE1α-dependent decay (RIDD).[11]

However, although a role of the ER stress regulator XBP1 in coordinating DNA damage repair has been proposed, a clear genetic link demonstrating XBP1 function in DDR and consecutive epithelial carcinogenesis is still missing. Here, we set out to directly assess the role of XBP1 in coordinating intestinal epithelial DDR and tumor suppression. We

§ Authors share co-senior authorship.

Abbreviations used in this paper: **4E-BP1, 4E-binding protein 1; AOM, azoxymethane; AraC, cytarabine A; CAC, colitis-associated colorectal cancer; CRC, colorectal cancer; DDIT4L, DNA damage inducible transcript 4-like; DDR, DNA damage response; DSS, dextran sodium sulfate; ER, endoplasmic reticulum; IEC, intestinal epithelial cell; IRE1, inositol-requiring enzyme type 1; KiMONo, Knowledge-gulded Multi-Omics Network; MDM2, mouse double minute 2; mTOR, mechanistic target of rapamycin; p-, phosphorylation; REDD2, regulated in development and DNA damage response 2; RER, ribonucleotide excision repair; RNaseH2, the ribonuclease H2; *Rnaseh2b* and RNASEH2B, ribonuclease H2, subunit B; TCGA, The Cancer Genome Atlas; TP53, tumor protein p53; UPR, unfolded protein response; XBP1, X-box binding protein 1.**

Most current article

0016-5085
https://doi.org/10.1053/j.gastro.2021.09.057

demonstrate that reduced *XBP1* expression in CRC is associated with poor long-term patient survival and reduced p53 pathway activity. Using mice double deficient for *Rnaseh2b* and *Xbp1* (*H2b/Xbp1*$^{\Delta IEC}$), in which both RER and ER stress control are selectively inhibited in the intestinal epithelium, we show that XBP1 maintains tumor suppression in a mechanism involving p53-dependent target gene expression.

Materials and Methods

Mice

Floxed *Xbp1* (*Xbp1*$^{fl/fl}$) or *Rnaseh2b* (*H2b*$^{fl/fl}$) mice were created as described previously.[2,12] *Villin-cre*$^{+}$;*Xbp1*$^{fl/fl}$ (*Xbp1*$^{\Delta IEC}$), *Villin-cre*$^{+}$;*Rnaseh2b*$^{fl/fl}$ (*H2b*$^{\Delta IEC}$), and *Villin-cre*$^{+}$;*Rnaseh2b*$^{fl/fl}$/*Xbp1*$^{fl/fl}$ (*H2b/Xbp1*$^{\Delta IEC}$) mice were backcrossed for at least 6 generations and used at an age of 8 to 12 weeks for all experiments with appropriate genotype littermate controls. All mice were maintained in a specific pathogen-free facility, and the quarterly health report did not indicate the presence of pathogenic species. Littermates of the same genotypes were cohoused. Mice were provided with food and water ad libitum and maintained in a 12-h light–dark cycle under standard conditions at Kiel University. Mice that underwent orthotopic transplantation of tumor organoids were housed in a specific pathogen-free facility at the Technische Universität München.

Genomic DNA of tail or ear biopsy samples of respective mouse strains was used for genotyping. For experiments including application of rapamycin or DSS, equal numbers (minimum n = 3 per genotype; see figure legends for details) of age-matched male and female animals were used. Procedures involving animal care were conducted conform to national and international laws and policies with appropriate permission. All experiments were performed in accordance with the Kiel University Guidelines for Animal Care and of the Technische Universität München Institutional Animal Care and Use Committees (Regierung von Oberbayern, Munich, Germany).

In Vivo Treatment of Mice

For DSS treatment, mice were supplied with 1% of DSS (MP Biomedical) dissolved in drinking water for 6 days, followed by 4 days of regular drinking water (acute models) or 1% DSS for 2 cycles of 7 or 5 days, followed by 14 days of regular drinking water (chronic models). Disease activity indices were obtained as described previously.[13] Consumption of drinking water was measured daily. For rapamycin treatment, *H2b*$^{\Delta IEC}$ or *H2b/Xbp1*$^{\Delta IEC}$ mice were injected intraperitoneally with 1.5 mg/kg body weight rapamycin (LC Laboratories, Hamburg, Germany) or dimethyl sulfoxide (Sigma-Aldrich) for 7 days before being humanely killed. For all experiments, histologic and histopathologic analyses were performed according to standard methods.

Histopathologic Analyses of Murine Intestinal Tissue

Postmortem, the small intestine and colon were excised and cut open longitudinally. The ileum and colon were rolled up as Swiss rolls from the distal to the proximal part and fixed in 10% formalin. Paraffin sections were cut and stained with H&E. Histologic scoring displays the combined score of inflammatory cell infiltration and tissue damage, as described elsewhere, and was performed in a blinded fashion by 2 independent observers, as described previously.[13]

Orthotopic Organoid Transplantation

Orthotopic transplantations of organoids were performed as previously described.[14] Briefly, organoids were dissociated into 5- to 10-cell clusters and resuspended in a minimal medium (advanced Dulbecco's modified Eagle medium/F12 containing 1× B27, 1× N2, L-glutamine [all from Gibco, Thermo Fisher Scientific], 10% Matrigel [Corning], 1% penicillin/streptomycin, and 10 μmol/L Y-27632 [STEMCELL Technologies]). For every injection (2–3 per mouse), 50 dissociated organoids in a volume of 80 μL were prepared.

Subsequently, the colon of the anesthetized mice was gently rinsed with phosphate-buffered saline using a syringe and a straight oral gavage needle. Colonoscopy of mice was performed using a rigid endoscope from Karl Storz (1.9 mm in diameter) with linear Hopkins lens optics (ColoView System). For injections of organoids into the submucosa of the colon, a flexible fine needle (Hamilton; 33-gauge, custom length of 16 inches, custom point style of 4 at 45°) was used. Injections that were correctly applied into the submucosa led to the formation of a bubble that closes the intestinal lumen.

Histologic Grading of Intestinal Tumors

All identifiable adenomas and invasive adenocarcinomas were classified in analogy to the recent World Health Organization Classification of Tumors of the Digestive System (Fifth Edition). Invasive adenocarcinomas were graded into low and high grade according to the extent of gland formation. The grade of dysplasia/intraepithelial neoplasia of small intestinal adenomas was classified into low- and high-grade intraepithelial neoplasia/dysplasia based on the degree of architectural complexity, extent of nuclear stratification, and severity of abnormal nuclear morphology.

Transcriptome Analysis

RNA sequencing was conducted on small intestinal organoids derived from *H2b/Xbp1*$^{fl/fl}$, *H2b*$^{\Delta IEC}$, *Xbp1*$^{\Delta IEC}$, *H2b/Xbp1*$^{\Delta IEC}$, and *H2b/p53*$^{\Delta IEC}$ mice (n = 3). Samples were sequenced on Illumina HiSeq3000 (Illumina, San Diego, CA) using Illumina total RNA stranded TruSeq protocol (Gene Expression Omnibus Project Accession No.182353). An average of ∼12 million 50-nucleotide unpaired-end reads was sequenced for each sample. Raw reads were preprocessed using Cutadapt[15] to remove adapter and low-quality sequences and then aligned to the Genome Reference Consortium Mouse Build 37 reference genome with TopHat2.[16] Gene expression values of the transcripts were computed by HTseq,[17] before differential gene expression levels were analyzed and visualized by the Bioconductor package DESeq2.[18] Generalized linear models were used to compare transcriptomes of *H2b*$^{\Delta IEC}$, *Xbp1*$^{\Delta IEC}$, *H2b/Xbp1*$^{\Delta IEC}$, or *H2b/p53*$^{\Delta IEC}$ organoids to *H2b/Xbp1*$^{fl/fl}$ organoids ($P < .05$). To interpret the biological significance of differential gene expression, Gene Ontology and Kyoto Encyclopedia of Genes and Genomes enrichment analyses were performed using the InnateDB database.[19]

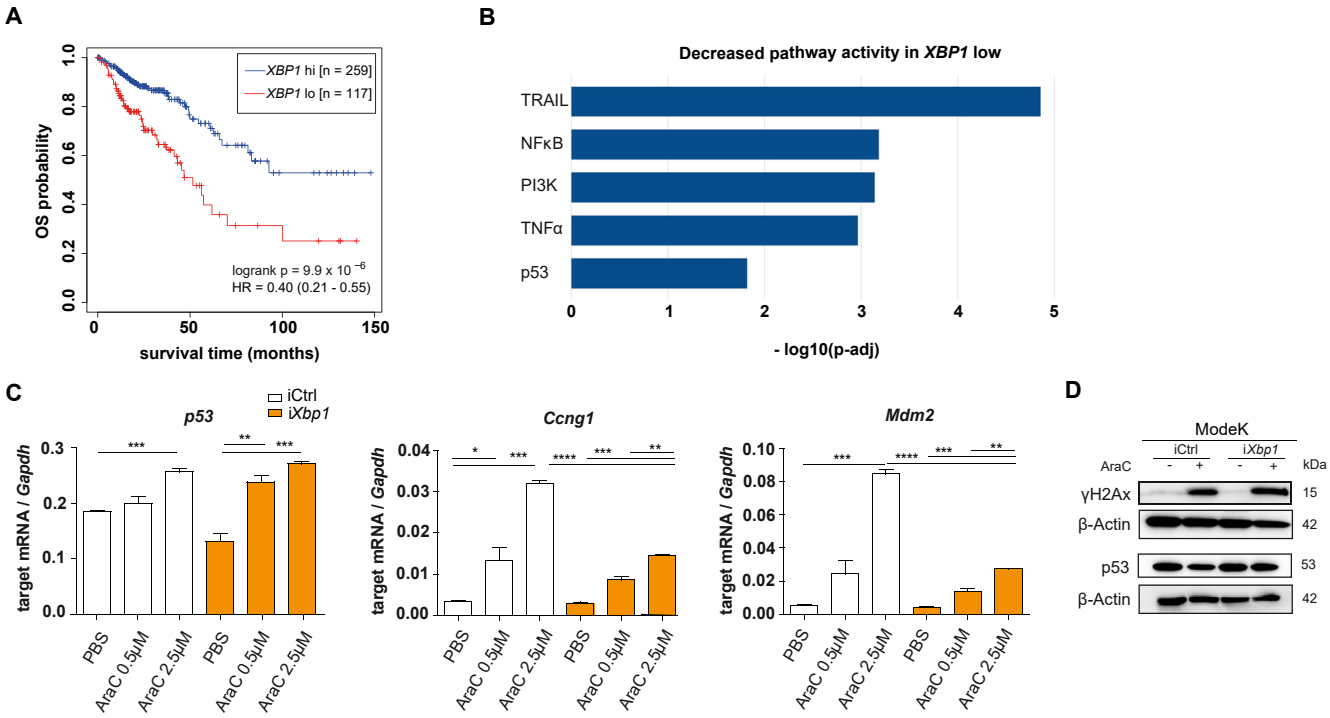

Figure 1. *XBP1* expression signature associates with CRC prognosis. (*A*) RNA expression data retrieved from the TCGA database (COAD—Colon Adenocarcinoma and READ—Rectum Adenocarcinoma) were used for overall survival (OS) analysis based on high or low *XBP1* expression in tumor samples. (*B*) Pathway RespOnsive GENes (PROGENy) analysis based on pathway enrichment analysis within the same COAD READ data set and shown as decreased pathway activity in *XBP1* low data set. NFκB, nuclear factor-κB; P13K, phosphoinositide 3-kinase; TRAIL, necrosis factor-related apoptosis-inducing ligand; TNF, tumor necrosis factor. (*C*) ModeK cells, treated with phosphate-buffered saline (PBS), 0.5 μmol/L and 2.5 μmol/L AraC for 24 hours. Quantitative real-time polymerase chain reaction analysis of p53-dependent target genes (sestrin 2 [*Sesn2*], cyclin G1 [*Ccng1*], and *Mdm2*), representative of a minimum of 3 individual experiments with 3 technical replicates. Relative messenger RNA (mRNA) expression is normalized to glyceraldehyde-3-phosphate dehydrogenase (*Gapdh*). Data are expressed as mean ± standard error of the mean, and significance was determined using an unpaired Student *t* test. (*D*) ModeK cells, stimulated with 2.5 μmol/L AraC for 24 hours. Protein lysates were probed against antibodies for p53, the phosphorylated form of H2A histone family member X (γH2Ax), and β-actin as a loading control on different Western blot membranes, representative of 3 individual experiments. $^{*}P < .05$, $^{**}P < .01$, $^{***}P < .0001$, $^{****}P < .00001$.

Multiomics-Based Network Inference Analysis

We obtained the CRC subset of The Cancer Genome Atlas (TCGA)[20] collection as an independent multiomics data set. It contains information of 101 patients with CRC measured across 4 omics levels, transciptome, proteome, methylation, and mutation. These data were used as an input for KiMONo (Knowledge-guIded Multi-Omics Network), a knowledge-guided multiomics network inference method, to infer a CRC specific multiomics network.[21] The resulting network served as blueprint to detect all multiomics features associated to mechanistic target of rapamycin (mTOR) pathway genes or XBP1, TP53, and DNA damage inducible transcript 4-like (DDIT4L). In a final step, we applied KiMONo to this trimmed data, detecting effects between the multiomics features including the mTOR pathway, XBP1, TP53, and DDIT4L.

Results

Low XBP1 *Expression Associates With Poor Colorectal Cancer Prognosis*

We correlated the expression of *XBP1* with long-term survival of patients with CRC (COAD [Colon Adenocarcinoma] and READ [Rectum Adenocarcinoma] data sets) in a data set publicly available through The Cancer Genome Atlas (TCGA)[20] and found that low *XBP1* expression was significantly associated with poor survival (Figure 1*A*). To identify a potential mechanism by which XBP1 contributes to tumor suppression in CRC, we performed pathway enrichment analysis. Based on *XBP1* expression (high vs low), we estimated the activity of 14 cancer-related pathways, including tumor necrosis factor-α, nuclear factor-κB, hypoxia, tumor necrosis factor-related apoptosis-inducing ligand (TRAIL), and p53-mediated DDR using Pathway RespOnsive GENes (PROGENy)[22] and observed that low *XBP1* expression was significantly associated with lower p53 pathway activity (Figure 1*B*).

To test whether XBP1 interferes with p53-coordinated DDR in intestinal epithelial cells (IECs), we stimulated murine small intestinal iCtrl or *Xbp1*-silenced (i*Xbp1*) ModeK cells with the DNA-damaging agent cytarabine A (AraC).[23] We assessed canonical p53 activation in response to DNA damage by analyzing the gene expression of *p53* and its target genes (cyclin G1 [*Ccng1*], mouse double minute 2 [*Mdm2*], sestrin 2 [*Sesn2*]) in AraC-stimulated ModeK cells

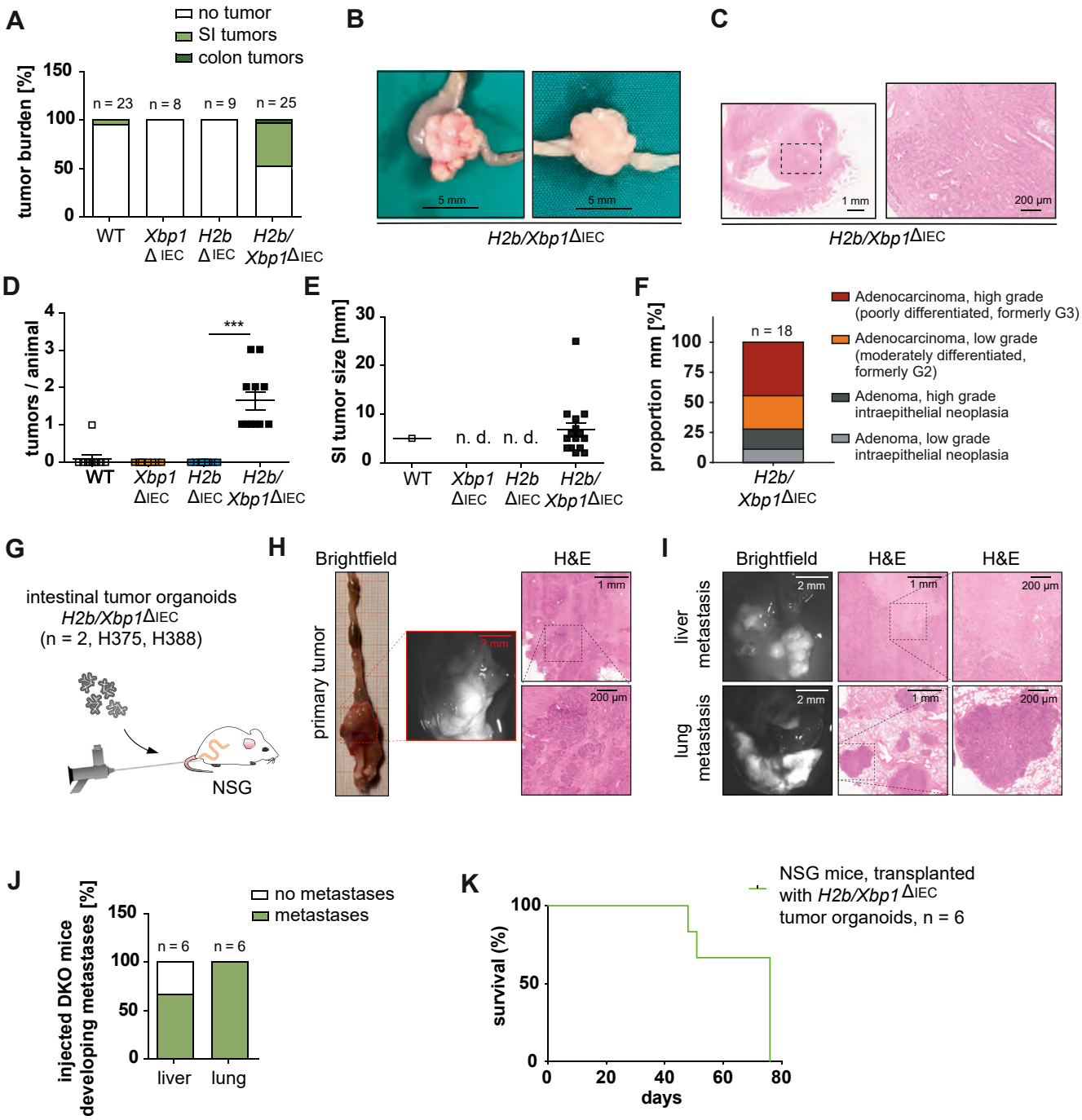

Figure 2. *Xbp1* deficiency drives spontaneous tumor development in *H2b/Xbp1*$^{\Delta IEC}$ mice. Tumor burden of 52-week-old wild-type (WT) mice (n = 23; 6 females, 17 males), *Xbp1*$^{\Delta IEC}$ mice (n = 8; 1 female, 7 males), *H2b*$^{\Delta IEC}$ mice (n = 9; 4 females, 6 males), and *H2b/Xbp1*$^{\Delta IEC}$ mice (n = 25; 15 females, 10 males). (*A*) Percentage of mice developing tumors with (*B*) representative images, and (*C*) representative H&E staining of invasive intestinal carcinomas from *H2b/Xbp1*$^{\Delta IEC}$ mice. (*D*) Mean number of small-intestine (SI) tumors per animal. ***$P < .0001$. (*E*) Size of SI tumors. (*F*) Histopathologic grading of SI mucosa from *H2b*$^{\Delta IEC}$ and *H2b/Xbp1*$^{\Delta IEC}$ mice. (*G*) NSG mice (n = 6; 4 females, 2 males) underwent orthotopic transplantation with *H2b/Xbp1*^{DIEC}-derived intestinal organoids (n = 2 clones). (*H*) Representative photograph of a primary tumor and photomicrograph of hepatic/pulmonary metastasis resulting from organoid transplantation. (*I*) H&E staining of tumors. (*J*) Percentage of hepatic or pulmonary metastases of mice who received implants. Scale bars, brightfield, 2 mm; H&E overview, 1 mm; H&E inset, 200 μm. (*K*) Kaplan-Meier survival curve of NSG mice after organoid transplantation. Data are expressed as mean ± standard error of the mean, and significance was determined using an unpaired Student *t* test. *H2b/Xbp1*$^{\Delta IEC}$ organoids are abbreviated as "DKO."

(iCtrl vs i*Xbp1*). i*Xbp1* cells presented with significantly impaired upregulation of p53-target genes in response to AraC treatment (Figure 1*C*), pointing to an involvement of XBP1 in p53 activation. Notably, reduced activation of p53-downstream targets in i*Xbp1* cells was not dependent on altered p53 protein expression in response to AraC

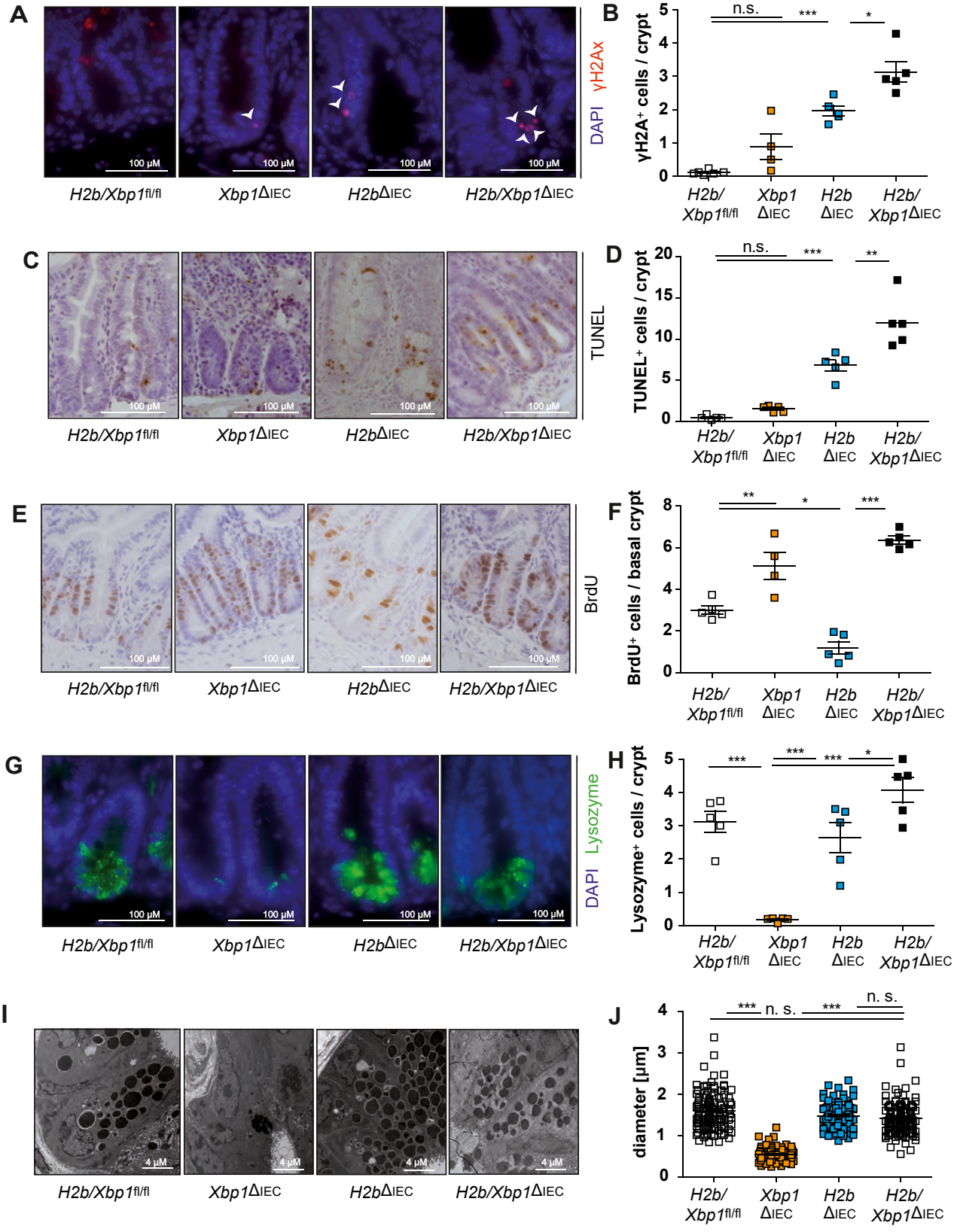

treatment (Figure 1*D*). Altogether, these data point toward a role of *Xbp1* in coordinating p53-driven DDRs in the intestinal epithelium.

Xbp1 *Deficiency Drives Spontaneous Intestinal Carcinogenesis*

To test whether absence of *Xbp1* phenocopies *p53* deletion and drives intestinal carcinogenesis in vivo, we took advantage of $H2b^{\Delta IEC}$ mice, a model of chronic DNA damage in which intestinal tumor formation occurs in the context of simultaneous knockout of epithelial p53 ($H2b/p53^{\Delta IEC}$ mice). We generated mice with a conditional intestinal epithelial deletion for both *Xbp1* and *Rnaseh2b* (hereafter $H2b/Xbp1^{\Delta IEC}$ mice) in addition to wild-type ($H2b/Xbp1^{fl/fl}$) and single-knockout animals ($Xbp1^{\Delta IEC}$ and $H2b^{\Delta IEC}$). Quantitative polymerase chain reaction and Western blot analysis of small intestinal organoids, derived from purified IECs, verified epithelial-specific conditional deletion of *Xbp1* and *Rnaseh2b* (Supplementary Figure 1). To assess the impact on spontaneous carcinogenesis, mice were aged, humanely killed at the age of 52 weeks, and overall tumor burden was evaluated. Whereas there was almost a complete lack of spontaneous tumor formation in $H2b/Xbp1^{fl/fl}$ (n = 1 of 23), $Xbp1^{\Delta IEC}$ (n = 0 of 8), and $H2b^{\Delta IEC}$ (n = 0 of 9) mice, 48% (n = 12 of 25) of $H2b/Xbp1^{\Delta IEC}$ mice developed spontaneous stenosing, predominantly small intestinal tumors (Figure 2*A*–*C*). On average, tumor-bearing mice presented with 1.5 tumors/intestine, ranging from 0.2 to 2.5 cm in size (Figure 2*D* and *E*).

Histopathologically, macroscopic tumors presented as low-/high-grade intraepithelial neoplasia or as invasive adenocarcinomas, of which most were high-grade adenocarcinomas (Figure 2*F*). Molecular phenotyping of $H2b/Xbp1^{\Delta IEC}$ tumor organoids unveiled upregulation of the Wnt target genes *Ccnd1*, *Cd44*, and *Sox9*, pointing to a direct interaction of XBP1 and Wnt/β-catenin signaling.[24,25] Importantly, this upregulation appeared to be dependent on autonomous release of Wnt ligands, because the pharmacologic Wnt secretion inhibitor IWP-2 failed to abrogate *Ccnd1*, *Cd44*, and *Sox9* expression in $H2b/Xbp1^{\Delta IEC}$-derived tumor organoids compared with nontumor $H2b/Xbp1^{\Delta IEC}$-derived organoids (Supplementary Figure 2).

To minimize the possibility that the observed phenotype of $H2b/Xbp1^{\Delta IEC}$ mice is primarily driven by microbial influences, we assessed both single ($H2b/Xbp1^{\Delta IEC}$) and cohoused ($H2b/Xbp1^{\Delta IEC}$ vs $H2b/Xbp1^{fl/fl}$) 52-week-old $H2b/Xbp1^{\Delta IEC}$ mice and found no differences in tumor incidence between groups (Supplementary Figure 3). To further investigate whether malignant properties are conserved outside of the mucosal microenvironment, we performed orthotopic colonoscopy-guided transplantation of $H2b/Xbp1^{\Delta IEC}$-derived tumor organoids (n = 2 clones) into the colonic mucosa of immunodeficient NSG (n = 6) mice (Figure 2*G*). We observed all 6 mice presented with locally invasive carcinomas at the site of injection (Figure 2*H* and *I*). Although in this model, metastases are rare events,[26,27] 4 of 6 mice (66%) presented with liver metastasis and all 6 mice (100%) presented with lung metastasis (Figure 2*J*), leading to overall rapid clinical deterioration (Figure 2*K*).

Xbp1 *Deficiency Fuels Epithelial DNA Damage and Compromises DNA Damage-Dependent Stem Cell Suppression In Vivo*

To further investigate spontaneous carcinogenesis in $H2b/Xbp1^{\Delta IEC}$ mice, we assessed morphologic changes in the small intestine of $H2b/Xbp1^{\Delta IEC}$ and $H2b^{\Delta IEC}$ non–tumor-bearing mice of the same experimental group (52 weeks). Macroscopically, $H2b/Xbp1^{\Delta IEC}$ animals presented with decreased body weight and increased small intestinal length (Supplementary Figure 4*A*).

Epithelial DNA damage, cell death, and proliferation were assessed using immunohistochemical and fluorescence staining for Ki67, 5-bromo-2′-deoxyuridine, the phosphorylated form of H2A histone family member X (γH2Ax), and terminal deoxynucleotidyl transferase–mediated deoxyuridine triphosphate nick-end labeling of the small intestine of non–tumor-bearing aged mice. Compared with $H2b^{\Delta IEC}$ mice, $H2b/Xbp1^{\Delta IEC}$ animals presented with heightened levels of DNA damage (Figure 3*A* and *B*), augmented epithelial cell death (Figure 3*C* and *D*), and elevated epithelial proliferation (Figure 3*E* and *F*). We also found that expansion of basal crypt proliferation in $H2b/Xbp1^{\Delta IEC}$ mice coincided with a nearly complete reconstitution of Paneth cells, pointing toward a role of Paneth cells in providing the niche for intestinal stem cells in the context of epithelial DNA damage (Figure 3*G*–*J*). Notably, young (8- to 12-week-old) mice of the indicated genotypes presented with a nearly complete phenocopy of the aged mice, albeit to a lesser degree (Supplementary Figures 4*B* and 5). We further validated that *Xbp1* knockdown in vitro enhanced DNA damage-induced epithelial cell death (Supplementary Figure 6*A*–*G*) and that young $H2b/Xbp1^{\Delta IEC}$ intestinal

Figure 3. *Xbp1* deficiency limits intestinal epithelial regeneration in the context of DNA damage in vivo. Representative images of the small intestine of 52-week-old $H2b/Xbp1^{fl/fl}$ (n = 5; 1 female, 4 males), $Xbp1^{\Delta IEC}$ (n = 5; 2 females, 3 males), $H2b^{\Delta IEC}$ (n = 5; 2 females, 3 males), and $H2b/Xbp1^{\Delta IEC}$ (n = 5; 2 females, 3 males) mice, stained for (A) phosphorylated form of H2A histone family member X (γH2Ax), with *white arrowheads* indicating $\gamma H2Ax^{+}$-nuclei, (*C*) terminal deoxynucleotidyl transferase–mediated deoxyuridine triphosphate nick-end labeling (TUNEL), (*E*) 5-bromo-2′-deoxyuridine (BrdU), and (*G*) lysozyme and the respective statistical analysis in which (*B*) $\gamma H2Ax^{+}$, (*D*)$TUNEL^{+}$, (*F*) $BrdU^{+}$, and (*H*) $lysozyme^{+}$ cells were assessed in 50 crypts. DAPI, 4′,6-diamidino-2-phenylindole. (*I*) Representative images and (*J*) diameter measurements of Paneth cell granule. Data are expressed as mean ± standard error of the mean, and significance was determined using 1-way analysis of variance . n.s., not significant; $^{*}P < .05$, $^{**}P < .01$, $^{***}P < .0001$.

organoids, compared with $H2b^{\Delta IEC}$ mice intestinal organoids, presented with increased colony forming numbers, thereby reflecting the observed in vivo phenotype (Supplementary Figure 6*H* and *I*).

Xbp1 *Deficiency Impairs DNA Damage-Driven Susceptibility to Experimental Enteritis*

We previously showed that loss of epithelial *Xbp1* drives small intestinal ileitis, which can be further exacerbated in a

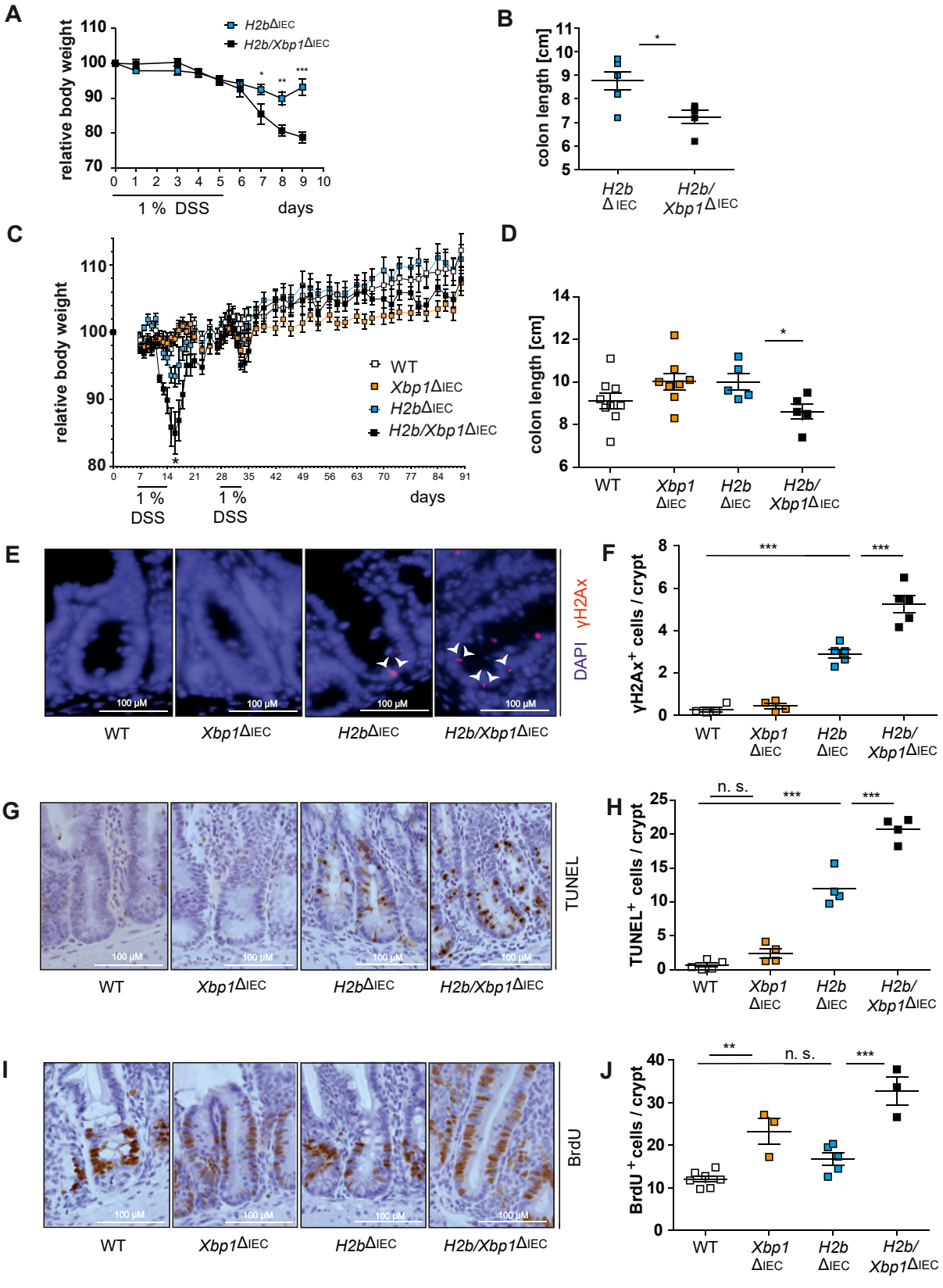

model of DSS exposure.[13,28] As *H2b/Xbp1*$^{\Delta IEC}$ mice presented with increased small intestinal cell death and DNA damage, we tested whether *Xbp1* and *Rnaseh2* deletions synergistically fuel intestinal inflammation by using an acute and chronic DSS exposure model. As indicated by the weight loss curve (Figure 4*A* and *C*) and colon length (Figure 4*B* and *D*), *H2b/Xbp1*$^{\Delta IEC}$ animals suffered from increased susceptibility toward acute and chronic DSS exposure. To specifically investigate whether impaired ER stress resolution and chronic DNA damage predominantly drive small intestinal inflammation, we assessed disease severity in DSS-treated *H2b/Xbp1*$^{\Delta IEC}$ animals by histopathologic scoring of the inflamed small intestine from acute (Supplementary Figure 7*A* and *B*) and chronic DSS exposure (Supplementary Figure 7*C* and *D*). In both models, we observed increased histopathologic disease severity in *H2b/Xbp1*$^{\Delta IEC}$ animals compared with control animals. Of note, we did not observe tumor formation in the chronic enteritis model.

We further delineated the molecular entity of small intestinal inflammation from the chronic DSS exposure model and noticed enhanced epithelial DNA damage (Figure 4*E* and *F*), increased cell death (Figure 4*G* and *H*), and epithelial proliferation in the small intestine of *H2b/Xbp1*$^{\Delta IEC}$ mice, as assessed by crypt 5-bromo-2′-deoxyuridine staining (Figure 4*I* and *J*). Altogether, our data implicate that *Xbp1* deficiency further aggravates chronic DNA damage-driven enteritis.

X-Box Binding Protein 1 Coordinates DNA Damage Response Via DNA Damage Inducible Transcript 4-Like/4E-Binding Protein 1

H2b/Xbp1$^{\Delta IEC}$ mice display a phenotype of ongoing epithelial proliferation despite overt DNA damage, reminiscent of the phenotype of *H2b/p53*$^{\Delta IEC}$ mice.[7] As our in vitro data indicate a role for XBP1 in coordinating DNA damage-induced p53 responses, we tested whether XBP1 and p53 are part of a common signaling pathway to coordinate DDR in IEC. We performed RNA sequencing of intestinal organoids generated from *H2b/Xbp1*$^{fl/fl}$, *H2b*$^{\Delta IEC}$, *Xbp1*$^{\Delta IEC}$, *H2b/Xbp1*$^{\Delta IEC}$, and *H2b/p53*$^{\Delta IEC}$ animals. Acquired data were used to identify unique and overlapping gene networks between *H2b/Xbp1*$^{\Delta IEC}$ and *H2b/p53*$^{\Delta IEC}$ intestinal organoids compared with the *H2b*$^{\Delta IEC}$ transcriptome (Figure 5*A*). We detected 353 (down: 139; up: 214) differentially expressed genes to be common between *H2b/Xbp1*$^{\Delta IEC}$ and *H2b/p53*$^{\Delta IEC}$ (Figure 5*B*). In contrast, 3435 genes were uniquely upregulated or downregulated in *H2b/p53*$^{\Delta IEC}$, and 1024 genes were uniquely upregulated or downregulated in *H2b/Xbp1*$^{\Delta IEC}$ intestinal organoids (Figure 5*B*) compared with *H2b*$^{\Delta IEC}$ cultures. Based on ranked lists of the top 50 differentially downregulated transcripts from the individual comparisons, we identified *Ano3*, *Ddit4l*, *Fam212*, and *Mcam* as saliently downregulated genes shared between the respective genotypes (*H2b/Xbp1*$^{\Delta IEC}$ and *H2b/p53*$^{\Delta IEC}$ vs *H2b*$^{\Delta IEC}$) (Supplementary Figure 8).

DDIT4L, also known as regulated in development and DDR 2 (REDD2), acts as an upstream inhibitor of mTOR signaling in various cell types, including cardiomyocytes, muscle cells, and neurons.[29,30] As mTOR is known to direct cell proliferation via the eukaryotic translation initiation factor 4E-binding protein 1 (4E-BP1), we hypothesized that regulation of DDIT4L might be involved in the formation of the hyperproliferative *H2b/Xbp1*$^{\Delta IEC}$ phenotype. Indeed, downregulation of *Ddit4l* transcript levels was preserved in small intestinal crypts of aged *H2b/Xbp1*$^{\Delta IEC}$ mice (Figure 5*C*). To delineate the cross talk between XBP1 and p53 in this context, we treated ModeK cells (iCtrl vs i*Xbp1*, transfected with small interfering RNA against *p53*) with AraC or the endogenous MDM2 inhibitor Nutlin. Nutlin induces nuclear translocation of p53 and leads to subsequent activation of p53-dependent gene expression, thereby serving as a positive control of p53 activation in the absence of DNA damage. We confirmed that (1) *Xbp1*-deficient cells showed impaired *Ddit4l* upregulation in response to Nutlin or Ara-C treatment (Figure 5*D*) and (2) *Ddit4l* expression essentially requires p53 (Figure 5*E*), further underscoring the cross talk between p53 and Xbp1 in coordinating *Ddit4l* expression. Hence, we reasoned that high *Ddit4l* expression in *H2b*$^{\Delta IEC}$ mice might inhibit mTOR activity, thereby causing a halt on stem cell proliferation, whereas downregulated *Ddit4l* levels in *H2b/Xbp1*$^{\Delta IEC}$ mice might evoke uncontrolled proliferation.

Because mTOR inhibition acts downstream via dephosphorylation of 4E-BP1, we assessed the phosphorylation (p-) status of 4E-BP1 in all 4 genotypes. Indeed, p-4E-BP1 levels were significantly decreased in the crypt region of *H2b*$^{\Delta IEC}$ animals but restored in *H2b/Xbp1*$^{\Delta IEC}$ and *H2b/p53*$^{\Delta IEC}$ mice (Figure 5*F* and *G*). This finding was further confirmed by Western blots using protein lysates of ModeK cells transfected with small interfering RNA against *Rnaseh2b* (Figure 5*H*), of small intestinal organoids (Figure 5*I*), or of isolated small intestinal crypts (Figure 5*J*). Again, *Rnaseh2b*-silenced ModeK cells or *H2b*$^{\Delta IEC}$ animals

Figure 4. Deletion of *Xbp1* heightens susceptibility towards DSS-induced colitis. (*A*) Weight curve and (*B*) colon length from acute DSS-induced colitis with age-matched *H2b*$^{\Delta IEC}$ (n = 6; 1 female, 5 males) and *H2b/Xbp1*$^{\Delta IEC}$ (n = 6; 3 females, 3 males) animals. (*C*) Weight curve and (*D*) colon length from chronic DSS-induced colitis with age-matched wild-type (WT) (n = 9; 5 females, 4 males), *Xbp1*$^{\Delta IEC}$ (n = 8; 4 females, 4 males), *H2b*$^{\Delta IEC}$ (n = 5; 2 females, 3 males), and *H2b/Xbp1*$^{\Delta IEC}$ (n = 5; 4 females, 1 male) mice. Representative images of the small intestine for (*E*) the phosphorylated form of H2A histone family member X (γH2Ax), with *white arrowheads* indicating γH2Ax^{+} nuclei, (*G*) terminal deoxynucleotidyl transferase–mediated deoxyuridine triphosphate nick-end labeling (TUNEL), and (*I*) 5-bromo-2′-deoxyuridine (BrdU) and the accompanying statistical analyses of (*F*) γH2Ax^{+}, (*H*) TUNEL^{+}, and (*J*) BrdU^{+} cells in the respective genotypes. DAPI, 4′,6-diamidino-2-phenylindole. Data are expressed as mean ± standard error of the mean, and significance was determined using (*A–D*) unpaired Student *t* test or (*E–J*) 1-way analysis of variance. *$P < .05$, **$P < .01$, ***$P < .0001$.

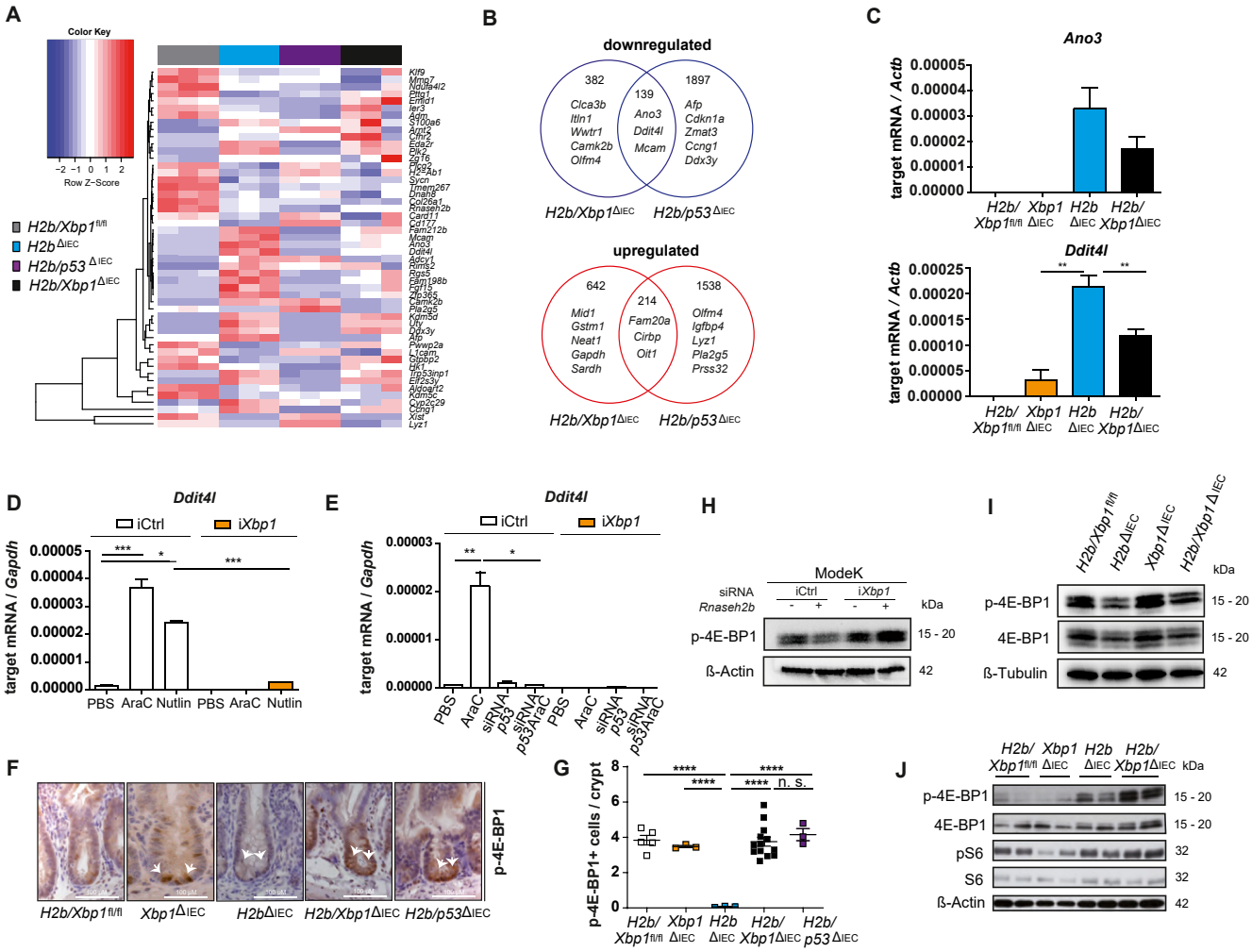

Figure 5. XBP1 regulates regenerative DDR in a DDIT4L-mTOR–dependent manner. (*A*) RNA sequencing of 3 organoid samples from 3 individual animals. (*B*) Venn diagram of uniquely and commonly regulated genes in intestinal organoids of *H2b/Xbp1*$^{\Delta IEC}$ and *H2b/p53*$^{\Delta IEC}$ vs *H2b*$^{\Delta IEC}$ mice. (*C*) Quantitative real-time polymerase chain reaction (qRT-PCR) analysis of small intestinal crypt cells of 52-week-old *H2b/Xbp1*$^{fl/fl}$ (n = 3, 3 males), *Xbp1*$^{\Delta IEC}$ (n = 6; 1 female, 5 males), *H2b*$^{\Delta IEC}$ (n = 6; 2 females, 4 males), and *H2b/Xbp1*$^{\Delta IEC}$ (n = 5; 2 females, 3 males) mice. mRNA, messenger RNA. qRT-PCR analysis of (*D*) ModeK cells, treated with phosphate buffered saline (PBS), 2.5 μmol/L AraC, or 50 μmol/L Nutlin for 24 hours, and (*E*) of ModeK cells transfected with small interfering (si)RNA control (iCtrl) and p53 and treated with phosphate-buffered saline (PBS) or 2.5 μmol/L AraC for 24 hours; both experiments representative of a minimum of 3 individual experiments with 3 technical replicates. Relative mRNA expression is normalized to *Actb* (β-actin) or glyceraldehyde-3-phosphate dehydrogenase (*Gapdh*). (*F*) Representative images (scale bar = 100 μM) and (*G*) statistical analysis of the p-4E-BP1–stained small intestine of 52-week-old *H2b/Xbp1*$^{fl/fl}$ (n = 3, 3 males), *Xbp1*$^{\Delta IEC}$ (n = 3; 1 female, 2 males), *H2b*$^{\Delta IEC}$ (n = 3; 1 female, 2 males), *H2b/Xbp1*$^{\Delta IEC}$ (n = 13; 8 females, 5 males), and *H2b*/p53$^{\Delta IEC}$ (n = 3; 3 males) mice. Western blots, representative of each of 3 individual experiments, of (*H*) ModeK cells transfected with small interfering RNA against *Rnaseh2b* for 24 hours, (*I*) untreated intestinal organoids of the indicated genotypes, and (*J*) small intestinal crypt cells from age-matched *H2b/Xbp1*$^{fl/fl}$ (2 females), *Xbp1*$^{\Delta IEC}$ (2 females), *H2b*$^{\Delta IEC}$ (1 female, 1 male), and *H2b/Xbp1*$^{\Delta IEC}$ (2 females) mice after exposure to chronic DSS colitis. β-Actin and β-tubulin served as loading controls. Data are expressed as mean ± standard error of the mean, and significance was determined using an unpaired Student *t* test (*D*, *E*) or 1-way analysis of variance (*G*).*$P < .05$, **$P < .01$, ***$P < .0001$, ****$P < .00001$.

displayed reduced p-4E-BP1 levels and phosphorylation was increased upon additional *Xbp1* deficiency. We additionally proved that DDIT4L and p53 coordinate 4E-BP1 phosphorylation, as knockdown of *p53* or *Ddit4l* in ModeK cells heightened p-4E-BP1 levels, whereas AraC-induced DNA damage decreased p-4E-BP1 levels in a DDIT4L-dependent manner (Supplementary Figure 9).

Multiomics Network Analysis of Colorectal Cancer Infers Interaction Between X-Box Binding Protein 1 and Tumor Protein p53 via Mechanistic Target of Rapamycin Signaling Pathway

Based on these data, we concluded that XBP1 cooperates with p53 to control cellular proliferation via DDIT4L-

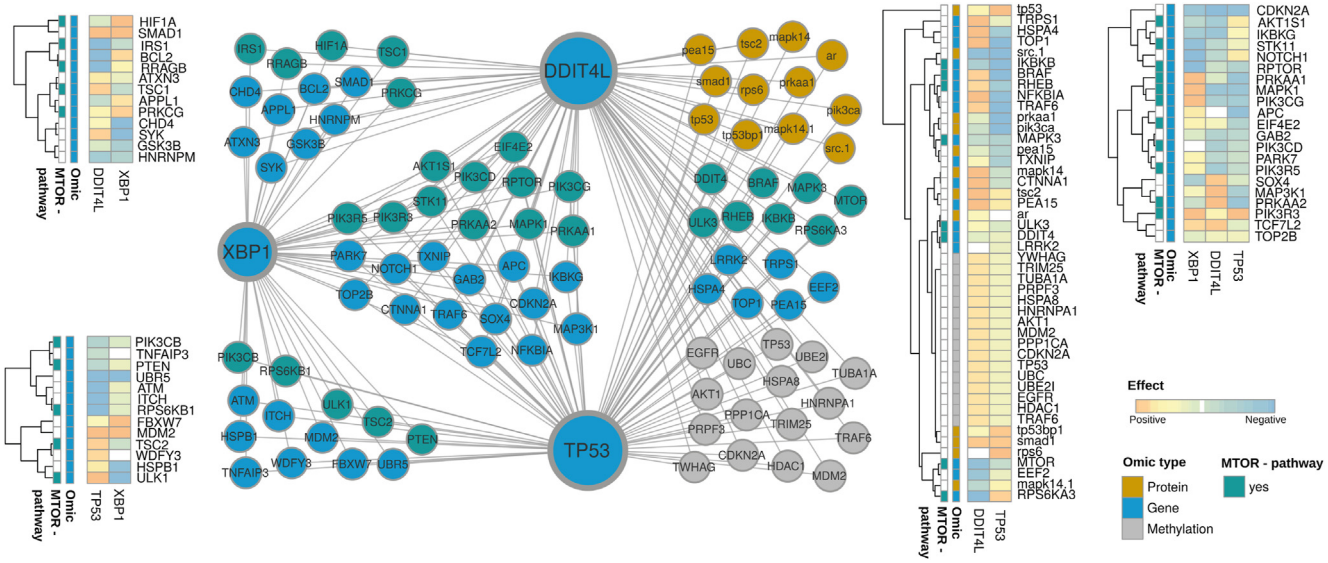

Figure 6. Inferred multiomic network based on TCGA colorectal cancer subset using the KiMONo algorithm. Within the network, nodes represent methylation sites (*gray*), proteins (*orange*,) and genes (*blue* and *turquoise*). Connections between the nodes denote statistical identified effects obtained via KiMONo. The heat maps on the side visualize the positive (*orange*) and negative (*blue*) effect strength between an omic feature, XBP1, TP53, and DDIT4L.

dependent mTOR signaling. To gain deeper insights whether XBP1 and TP53 are molecularly connected via the mTOR pathway in the clinical setting of CRC, we used the TCGA data set, in which 101 patients with CRC were assessed across 4 different omics levels: transcriptome (16,115 transcripts), proteome (130 proteins), mutations (39,674 positions), and methylation (2043 sites). Using the KiMONo network inference algorithm,[21] we were able to trim the multidimensional features with possible impact on XBP1, DDIT4L, TP53, and the mTOR pathway to 120 genes, 52 proteins, 70 mutation sites, and 346 methylation sites. Of these 588 features, KiMONo identified 47 features statistically affecting XBP1 and 80 features associated to TP53 and DDIT4L (Figure 6). Interestingly, we identified the gene expression of *MDM2*, a canonical p53 target gene, to be strongly affected by both XBP1 and p53, which is in line with the observed association of *XBP1* gene expression and p53 pathway activity shown in Figure 1. In addition, of 65 transcripts that were correlated with XBP1, DDIT4L, and p53 levels, and 29 were related to the mTOR pathway, including *EIF4E2*, which codes for the transcription factor regulated by 4E-BP1. Altogether, this network inference algorithm in a CRC data set strongly infers mTOR signaling as a crucial molecular executor of XBP1 and p53-mediated tumor suppression.

Extrinsic Mechanistic Target of Rapamycin Inhibition Reduces Phosphorylated 4E- Binding Protein 1 Levels and Impedes Hyperproliferation in H2b/Xbp1$^{\Delta IEC}$ *Mice*

Based on these findings, we hypothesized that inhibition of mTOR would reconstitute suppression of intestinal epithelial proliferation in *H2b/Xbp1*$^{\Delta IEC}$ mice, thereby providing an actionable therapeutic intervention. Thus, we interrogated the growth properties of intestinal organoids from all 4 genotypes (*H2b/Xbp1*$^{fl/fl}$, *Xbp1*$^{\Delta IEC}$, *H2b*$^{\Delta IEC}$, and *H2b/Xbp1*$^{\Delta IEC}$) using the CellTiter-Glo assay, which assesses the numbers of viable cells by quantifying adenosine 5′-triphosphate. We first validated that despite ongoing DNA damage, *H2b/Xbp1*$^{\Delta IEC}$ intestinal organoids showed significantly enriched cell viability compared with *H2b*$^{\Delta IEC}$ intestinal organoids (Supplementary Figure 10). We further assessed the suppressive capacity of mTOR treatment in the same experimental setting and observed that rapamycin most strongly inhibited the growth rate of *H2b/Xbp1*$^{\Delta IEC}$ intestinal organoids (Figure 7*A* and *B*). These findings were independently validated in *H2b*$^{\Delta IEC}$ and *H2b/Xbp1*$^{\Delta IEC}$ intestinal organoids using colony-forming assays (Figure 7*C*). Western blot analysis of intestinal organoids confirmed reduction of p-4E-BP1 in *H2b*$^{\Delta IEC}$ and *H2b/Xbp1*$^{\Delta IEC}$ intestinal organoids upon rapamycin treatment (Figure 7*D*).

To test whether mTOR inhibition might serve as a preventive mechanism to counterbalance proliferation in DNA-damaged IECs, we intraperitoneally treated age- and sex-matched *H2b*$^{\Delta IEC}$ and *H2b/Xbp1*$^{\Delta IEC}$ mice (n = 3–4/group) with rapamycin or dimethyl sulfoxide daily for 7 days. Rapamycin treatment significantly blocked epithelial hyperproliferation (Figure 7*E* and *F*), 4E-BP1 phosphorylation (Figure 7*G* and *H*), and cell death (Figure 7*I* and *J*) in *H2b/Xbp1*$^{\Delta IEC}$ mice. Taken together, these data show that XBP1 restricts cellular proliferation in response to DNA damage in IECs in a mechanism involving the DDIT4l/mTOR pathway.

Discussion

We demonstrate that XBP1 coordinates epithelial DDR in IECs and protects from tumorigenesis in a genetic model of chronic epithelial DNA damage. Clinical data from CRC

patients support a protective role of XBP1 on overall survival. Using pathway enrichment analysis, we show that low *XBP1* activation is significantly associated with decreased pathway activation of the tumor suppressor p53. It must, however, be noted that the reliable assessment of XBP1 protein is challenging in a global proteome data set, and

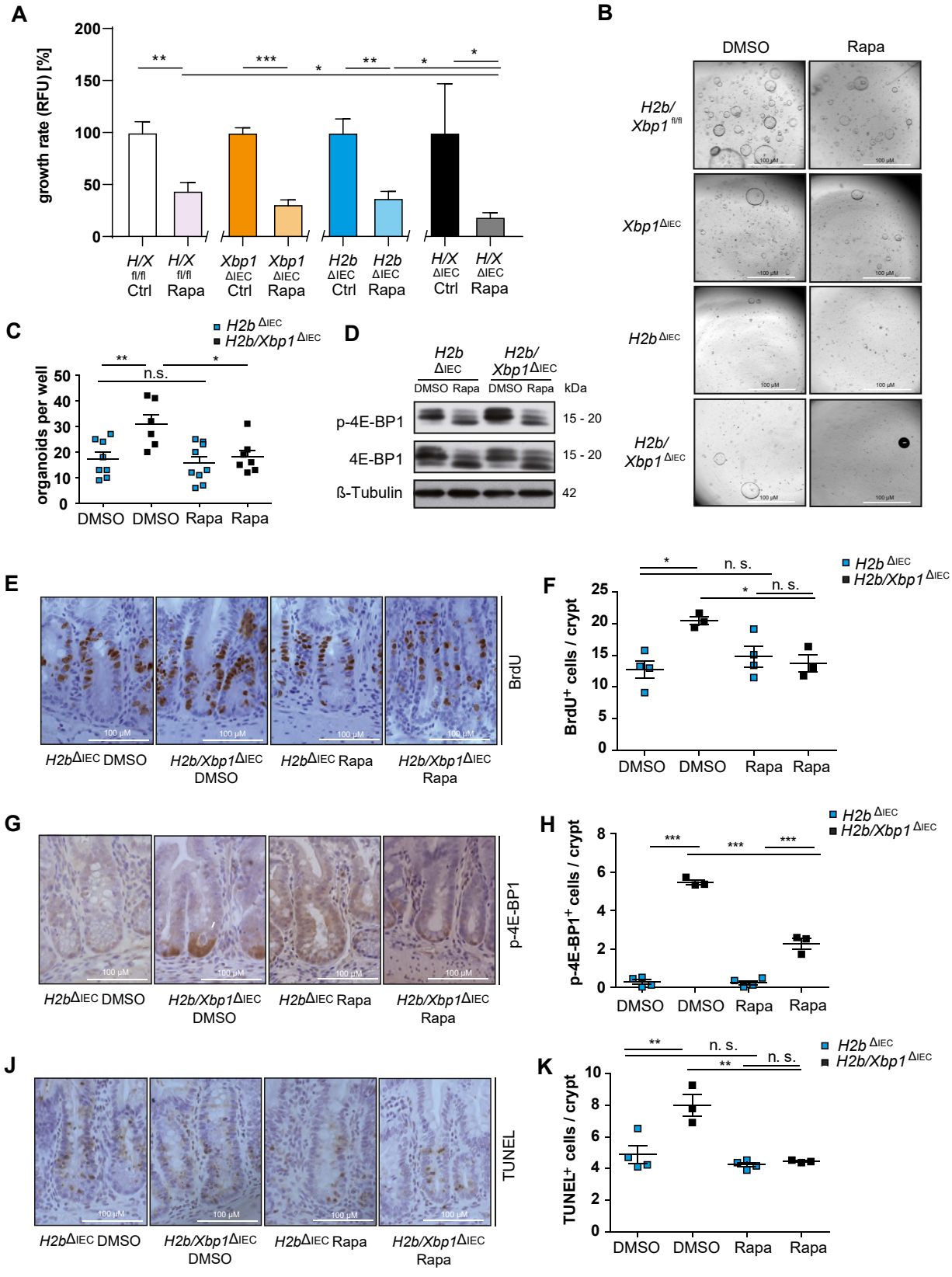

therefore, this finding still warrants further validation on the protein level. Associations between XBP1 and carcinogenesis have been described in clinical data sets, albeit with contradictory effects on the clinical outcome. XBP1 function has been shown to be associated with poor overall survival in triple-negative breast cancer and ovarian cancer.[31] In contrast, we here confirm and functionally delineate an epithelial-intrinsic tumor suppressive function of XBP1 in intestinal tumorigenesis.

The presented findings are in line with previous data published on XBP1 and colorectal carcinogenesis in which chemical models (AOM-DSS) and genetic models ($Apc^{Min/+}$) were used to show that epithelial *Xbp1* deletion led to intestinal hyperproliferation and subsequent increased adenoma formation. However, the exact molecular mechanism on how disrupted XBP1 transforms epithelial cells into a hyperproliferative state in response to genotoxic stress remained poorly understood.[2] Our data now support that XBP1 crucially supports p53 activity to direct stem cell suppression as a result to DNA damage.

Xbp1 deletion in the intestinal epithelium of mice induces a mild enteritis that turns into a fissuring, transmural inflammatory bowel disease–like ileitis when the autophagy gene *Atg16l1* is additionally deleted.[32] This inflammation instigates a highly regenerative process with hyperproliferative characteristics in which functioning DNA repair and p53-mediated DDRs are indispensable. It is therefore not surprising that *TP53* mutations commonly occur in chronically inflamed colonic epithelia of patients with inflammatory bowel disease.[33–35]

These initial *TP53* mutations in nonneoplastic mucosae or precancerous neoplasms lead to uncontrolled cell proliferation and to a concomitant accumulation of further mutations in oncogenes and tumor suppressor genes (ie, *KRAS* and *APC*) and may hence initiate a stepwise progression to CRC.[33] Interestingly, this so-called colitis-associated CRC pathway follows a reverse mutation sequence (*TP53-KRAS-APC*) compared with the classical CRC route that follows the Vogelstein model (*APC-KRAS-TP53*).[36,37] Of note, *TP53* mutations are rare in the adenomatous precursors of the classical CRC pathway, whereas mutations in *KRAS* and *APC* are less prevalent in colitis-associated CRC.[38]

Using the model of epithelial *Rnaseh2b* deficiency, we now show that $H2b/Xbp1^{\Delta IEC}$ mice present with aggressive, invasive, and metastatic adenocarcinoma. Notably, we did not find a strong indication for a modulating role of the intestinal microbiome in driving the carcinogenic phenotype, because tumor incidence was comparable between single-housed and cohoused ($H2b/Xbp1^{\Delta IEC}$ vs $H2b/Xbp1^{fl/fl}$) mice.

It must be noted that 96% of tumors arise in the small intestine, and therefore, conclusions on the pathogenesis of human CRC should be made with caution. Still, it needs to be pointed out that species-specific differences between mouse and human are also found (eg, in the $Apc^{Min/+}$ model),[39] in which mice predominantly display small-intestinal tumors. In line with this finding, our model shows that *Xbp1* deficiency confers a site-specific vulnerability to small-intestinal IECs resulting from the misled interplay of DNA damage and *Xbp1* deletion, which ultimately manifests into spontaneous carcinogenesis. We further observe that orthotopically transplanted intestinal organoids from $H2b/Xbp1^{\Delta IEC}$-derived tumors result in 100% tumor manifestation at the organoid injection site and in 66% liver and 100% lung respective metastasis formation. These findings point to a highly aggressive tumor entity in the form of metastasis formation, which has not yet been described in previous models of orthotopic tumor transplantation.[26,27]

Altogether, these data therefore provide the first in vivo proof that impairment of RER may indeed result in invasive and metastatic adenocarcinoma in vivo. This finding could have potential translational impact with regard to molecular-guided therapy in CRC, as it has been recently shown that the genome of cells with deficient RER display increased abundance of poly(adenosine diphosphate-ribose) polymerase-trapping lesions, which can be specifically targeted using poly(adenosine diphosphate-ribose) polymerase inhibitors.[40]

In an attempt to understand the underlying molecular mechanism, we identified *Ddit4l* as a p53-dependent regulator of stem cell suppression. Importantly, DDIT4L is the paralog of DDIT4, also known as REDD1, which among other functions acts as a p53-dependent DNA damage repair gene[41] and has previously been validated as prognostic marker in several malignancies.[42] Although our data do not directly imply a role of DDIT4L in DNA damage repair, it is conceivable that DDIT4L directs DNA damage repair methods via mTOR, which has previously been

Figure 7. Rapamycin abolishes DDIT4L-mediated hyperproliferation by inhibiting mTOR-dependent phosphorylation of 4E-BP1. (*A*) CellTiter-Glo assay and (*B*) representative images (scale bar = 100 μM) of small-intestinal organoids stimulated with dimethyl sulfoxide (DMSO; control) or 1 μmol/L rapamycin for 72 hours. Representative data of 3 individual experiments with 3 technical replicates. $H2b/Xbp1^{fl/fl/\Delta IEC}$ organoids are abbreviated as "$H/X^{fl/fl/\Delta IEC}$". (*C*) Colony formation assay of $H2b^{\Delta IEC}$ and $H2b/Xbp1^{\Delta IEC}$ intestinal organoids, treated with DMSO or 1 μmol/L rapamycin every other day over the time course of 10 days, representative of 3 experiments with 3 technical replicates. (*D*) Western blot of $H2b^{\Delta IEC}$ and $H2b/Xbp1^{\Delta IEC}$ intestinal organoids, treated with DMSO or 1 μmol/L rapamycin for 24 hours, representative of 3 experiments. β-Tubulin served as a loading control. Data are expressed as mean ± standard error of the mean, and significance was determined using an unpaired Student *t* test. Age-matched $H2b^{\Delta IEC}$ (n = 8; 5 females, 3 males) and $H2b/Xbp1^{\Delta IEC}$ (n = 6; 2 females, 4 males) mice received DMSO or 1.5 mg/kg body weight rapamycin intraperitoneally daily for 7 days. Representative images of the small intestine of DMSO- vs rapamycin-treated $H2b^{\Delta IEC}$ and $H2b/Xbp1^{\Delta IEC}$ mice for (*E*) 5-bromo-2′-deoxyuridine (BrdU) (scale bar = 100 μM), (*G*) p-4E-BP1 (scale bar = 100 μM), and (*I*) terminal deoxynucleotidyl transferase–mediated deoxyuridine triphosphate nick-end labeling (TUNEL) and accompanying statistical analysis for (*F*) $BrdU^+$, (*H*), p-4E-$BP1^+$ and (*J*) $TUNEL^+$ cells (scale bar = 100 μM). Data are expressed as mean ± standard error of the mean, and significance was determined using 1-way analysis of variance. $^*P < .05$, $^{**}P < .01$, $^{***}P < .0001$.

shown, for example, in the context of CRC[43] and pancreatic cancer.[44]

Taken together, our findings reveal a novel role of the intestinal epithelial XBP1 in coordinating epithelial DDR downstream of p53. *Xbp1* deletion disrupts a fundamental feedback mechanism that restricts epithelial proliferation via DDIT4L and 4E-BP1 and which might provide an actionable layer of cancer prevention and treatment in a subset of patients with insufficient p53 activity.

Supplementary Material

Note: To access the supplementary material accompanying this article, visit the online version of *Gastroenterology* at www.gastrojournal.org, and at https://doi.org/10.1053/j.gastro.2021.09.057.

References

1. Kaser A, Lee A-H, Franke A, et al. XBP1 links ER stress to intestinal inflammation and confers genetic risk for human inflammatory bowel disease. Cell 2008;134:743–756.
2. Niederreiter L, Fritz TMJ, Adolph TE, et al. ER stress transcription factor Xbp1 suppresses intestinal tumorigenesis and directs intestinal stem cells. J Exp Med 2013;210:2041–2056.
3. Schmitt M, Greten FR. The inflammatory pathogenesis of colorectal cancer. Nat Rev Immunol 2021;21:653–667.
4. Rad R, Cadiñanos J, Rad L, et al. A genetic progression model of Braf(V600E)-induced intestinal tumorigenesis reveals targets for therapeutic intervention. Cancer Cell 2013;24:15–29.
5. Bennecke M, Kriegl L, Bajbouj M, et al. Ink4a/Arf and oncogene-induced senescence prevent tumor progression during alternative colorectal tumorigenesis. Cancer Cell 2010;18:135–146.
6. Reijns MAM, Rabe B, Rigby RE, et al. Enzymatic removal of ribonucleotides from DNA is essential for mammalian genome integrity and development. Cell 2012;149:1008–1022.
7. Aden K, Bartsch K, Dahl J, et al. Epithelial RNase H2 maintains genome integrity and prevents intestinal tumorigenesis in mice. Gastroenterology 2019;156:145–159.e19.
8. Argemí J, Kress TR, Chang HCY, et al. X-box binding protein 1 regulates unfolded protein, acute-phase, and DNA damage responses during regeneration of mouse liver. Gastroenterology 2017;152:1203–1216.e15.
9. Yamamori T, Meike S, Nagane M, et al. ER stress suppresses DNA double-strand break repair and sensitizes tumor cells to ionizing radiation by stimulating proteasomal degradation of Rad51. FEBS Lett 2013;587:3348–3353.
10. Tao R, Chen H, Gao C, et al. Xbp1-mediated histone H4 deacetylation contributes to DNA double-strand break repair in yeast. Cell Res 2011;21:1619–1633.
11. Dufey E, Bravo-San Pedro JM, Eggers C, et al. Genotoxic stress triggers the activation of IRE1α-dependent RNA decay to modulate the DNA damage response. Nat Commun 2020;11:2401.
12. Hiller B, Achleitner M, Glage S, et al. Mammalian RNase H2 removes ribonucleotides from DNA to maintain genome integrity. J Exp Med 2012;209:1419–1426.
13. Aden K, Tran F, Ito G, et al. ATG16L1 orchestrates interleukin-22 signaling in the intestinal epithelium via cGAS-STING. J Exp Med 2018;215:2868–2886.
14. Roper J, Tammela T, Akkad A, et al. Colonoscopy-based colorectal cancer modeling in mice with CRISPR–Cas9 genome editing and organoid transplantation. Nat Protoc 2018;13:217–234.
15. Martin M. Cutadapt removes adapter sequences from high-throughput sequencing reads. EMBnet.journal 2011;17:10–12.
16. Trapnell C, Roberts A, Goff L, et al. Differential gene and transcript expression analysis of RNA-seq experiments with TopHat and Cufflinks. Nat Protoc 2012;7:562–578.
17. Anders S, Pyl PT, Huber W. HTSeq—a Python framework to work with high-throughput sequencing data. Bioinformatics 2014;31:166–169.
18. Love MI, Huber W, Anders S. Moderated estimation of fold change and dispersion for RNA-seq data with DESeq2. Genome Biol 2014;15:550.
19. Breuer K, Foroushani AK, Laird MR, et al. InnateDB: systems biology of innate immunity and beyond—recent updates and continuing curation. Nucleic Acids Res 2013;41:D1228–D1233.
20. Muzny DM, Bainbridge MN, Chang K, et al. Comprehensive molecular characterization of human colon and rectal cancer. Nature 2012;487:330–337.
21. Ogris C, Hu Y, Arloth J, et al. Versatile knowledge guided network inference method for prioritizing key regulatory factors in multi-omics data. Sci Rep 2021;11:6806.
22. Schubert M, Klinger B, Klünemann M, et al. Perturbation-response genes reveal signaling footprints in cancer gene expression. Nat Commun 2018;9:20.
23. Grant S. Ara-C: cellular and molecular pharmacology. Adv Cancer Res 1998;72:197–233.
24. Wang Q, Zou Y, Nowotschin S, et al. The p53 family coordinates Wnt and nodal inputs in mesendodermal differentiation of embryonic stem cells. Cell Stem Cell 2017;20:70–86.
25. Kwak B, Kim DU, Kim TO, et al. MicroRNA-552 links Wnt signaling to p53 tumor suppressor in colorectal cancer. Int J Oncol 2018;53:1800–1808.
26. Roper J, Tammela T, Cetinbas NM, et al. In vivo genome editing and organoid transplantation models of colorectal cancer and metastasis. Nat Biotechnol 2017;35:569–576.
27. Lannagan TRM, Lee YK, Wang T, et al. Genetic editing of colonic organoids provides a molecularly distinct and orthotopic preclinical model of serrated carcinogenesis. Gut 2019;68. 684 LP—692.
28. Tschurtschenthaler M, Adolph TE, Ashcroft JW, et al. Defective ATG16L1-mediated removal of IRE1α drives Crohn's disease–like ileitis. J Exp Med 2017;214:401–422.
29. Simonson B, Subramanya V, Chan MC, et al. DDiT4L promotes autophagy and inhibits pathological cardiac

hypertrophy in response to stress. Sci Signal 2017;10:eaaf5967.
30. Corradetti MN, Inoki K, Guan K-L. The stress-inducted proteins RTP801 and RTP801L are negative regulators of the mammalian target of rapamycin pathway. J Biol Chem 2005;280:9769–9772.
31. Chen X, Iliopoulos D, Zhang Q, et al. XBP1 promotes triple-negative breast cancer by controlling the HIF1α pathway. Nature 2014;508:103–107.
32. Adolph TE, Tomczak MF, Niederreiter L, et al. Paneth cells as a site of origin for intestinal inflammation. Nature 2013;503:272–276.
33. Baker A-M, Cross W, Curtius K, et al. Evolutionary history of human colitis-associated colorectal cancer. Gut 2019;68:985–995.
34. Brentnall TA, Crispin DA, Rabinovitch PS, et al. Mutations in the p53 gene: an early marker of neoplastic progression in ulcerative colitis. Gastroenterology 1994;107:369–378.
35. Yin J, Harpaz N, Tong Y, et al. p53 Point mutations in dysplastic and cancerous ulcerative colitis lesions. Gastroenterology 1993;104:1633–1639.
36. Itzkowitz SH, Yio X. Inflammation and cancer IV. Colorectal cancer in inflammatory bowel disease: the role of inflammation. Am J Physiol Liver Physiol 2004;287:G7–G17.
37. Fearon ER, Vogelstein B. A genetic model for colorectal tumorigenesis. Cell 1990;61:759–767.
38. Hao XP, Frayling IM, Sgouros JG, et al. The spectrum of p53 mutations in colorectal adenomas differs from that in colorectal carcinomas. Gut 2002;50:834–839.
39. Su LK, Kinzler KW, Vogelstein B, et al. Multiple intestinal neoplasia caused by a mutation in the murine homolog of the APC gene [published correction appears in Science 1992;256:1114]. Science 1992;256:668–670.
40. Zimmermann M, Murina O, Reijns MAM, et al. CRISPR screens identify genomic ribonucleotides as a source of PARP-trapping lesions. Nature 2018;559:285–289.
41. Janic A, Valente LJ, Wakefield MJ, et al. DNA repair processes are critical mediators of p53-dependent tumor suppression. Nat Med 2018;24:947–953.
42. Pinto JA, Rolfo C, Raez LE, et al. In silico evaluation of DNA damage inducible transcript 4 gene (DDIT4) as prognostic biomarker in several malignancies. Sci Rep 2017;7:1526.
43. Hsieh H-J, Zhang W, Lin S-H, et al. Systems biology approach reveals a link between mTORC1 and G2/M DNA damage checkpoint recovery. Nat Commun 2018;9:3982.
44. Müller D, Shin S, Goullet de Rugy T, et al. eIF4A inhibition circumvents uncontrolled DNA replication mediated by 4E-BP1 loss in pancreatic cancer. JCI Insight 2019;4:e121951.

Received December 7, 2020. Accepted September 23, 2021.

Correspondence
Address correspondence to: Konrad Aden, MD, Department of Internal Medicine I, University Medical Center Schleswig Holstein, Rosalind Franklin Straße 11, 24105 Kiel, Germany. e-mail: k.aden@ikmb.uni-kiel.de, or Philip Rosenstiel, MD, Institute of Clinical Molecular Biology, Christian-Albrechts-University Kiel, Rosalind Franklin Straße 11, 24105 Kiel, Germany. e-mail: p.rosenstiel@mucosa.de.

CRediT Authorship Contributions
Lina Welz, MD (Conceptualization: Lead; Investigation: Lead). Nassim Kakavand, MD (Investigation: Equal; Validation: Equal). Xiang Hang, MSc (Data curation: Equal; Formal analysis: Equal). Georg Laue (Conceptualization: Equal; Data curation: Equal; Formal analysis: Equal; Validation: Equal). Go Ito, MD PhD (Formal analysis: Lead). Miguel Gomes Silva, MSc (Data curation: Equal; Formal analysis: Equal). Christina Plattner, PhD (Data curation: Lead; Formal analysis: Lead). Neha Mishra, PhD (Formal analysis: Equal; Validation: Equal; Visualization: Equal). Felicitas Tengen, MSc (Formal analysis: Equal; Methodology: Equal; Visualization: Equal). Christoph Ogris, PhD (Methodology: Lead; Software: Lead). Moritz Jesinghaus, MD (Investigation: Lead). Felix Wottawa (Formal analysis: Equal; Resources: Equal). Philip Arnold, PhD (Formal analysis: Lead). Leena Kaikkonen, PhD (Investigation: Supporting). Stefanie Stengel, PhD (Investigation: Equal; Methodology: Equal). Florian Tran, MD (Investigation: Equal). Saumy Das, MD, PhD (Writing – review & editing: Supporting). Arthur Kaser, MD, PhD (Conceptualization: Supporting; Writing – original draft: Equal). Zlatko Trajanoski, PhD (Resources: Equal; Software: Equal). Richard Blumberg, MD, PhD (Conceptualization: Supporting; Writing – original draft: Equal). Christoph Roecken, MD (Data curation: Supporting; Resources: Equal). Dieter Saur, MD (Writing – review & editing: Supporting). Markus Tschurtschenthaler, PhD (Formal analysis: Equal; Investigation: Equal). Stefan Schreiber, MD (Conceptualization: Supporting; Writing – original draft: Supporting). Philip Rosenstiel, MD (Conceptualization: Lead; Writing – original draft: Lead). Konrad Aden, MD (Funding acquisition: Lead; Supervision: Lead; Writing – original draft: Lead; Writing – review & editing: Lead)

Conflicts of interest
The authors disclose no conflicts.

Funding
This work was supported by the Deutsche Forschungsgemeinschaft (DFG) Research Training Group 1743 (P.R.), the BMBF iTREAT project (P.R.), the DFG Cluster of excellence "Precision medicine in chronic inflammation" RTF III and TI-1, the DFG CRC 1371 P11 (Project-ID 395357507; M.T.), the Else Kröner-Fresenius-Stiftung (EKFS) research grant #2019_A09 (K.A.), the Wilhelm Sander-Stiftung #2019.046.1 (K.A.), the Bundesministerium für Bildung und Forschung (BMBF) (eMED Juniorverbund "Try-IBD" 01ZX1915A), the DFG RU5042 (P.R., K.A.), the National Institutes of Health/National Institute of Diabetes and Digestive and Kidney Diseases (grants DK044319, DK051362, DK053056 and DK088199; R.S.B.), DFG CRC877 A13 and Z2 (Project-ID 125440785; P.A.), the Austrian Academy of Sciences (C.P.), the European Research Council (grant 786295; Z.T.), and National Institute of Diabetes and Digestive and Kidney Diseases grant to the Harvard Digestive Diseases Center DK034854 (R.S.B). Sequencing was performed with help of the DFG Competence Centre for Genomic Analysis sequencing center at CAU Kiel.

Supplementary Materials and Methods

Complementary DNA Synthesis and Gene Expression Analysis

The RNeasy Kit (Qiagen, Hilden, Germany) was used to isolate messenger RNA from either ModeK cells washed in phosphate-buffered saline (PBS), from organoids after Matrigel (BD Biosciences, Heidelberg, Germany) was washed with PBS, or from snap-frozen tissue. Complementary (c)DNA was synthesized using the Revert Aid Premium cDNA Synthesis Kit (Fermentas, Waltham, MA) according to the manufacturer's protocol. To examine gene expression, cDNA samples were subjected to quantitative real-time polymerase chain reaction (PCR) using SYBR Green or TaqMan assays purchased from Applied Biosystems. Reactions were performed on the Applied Biosystems 7900HT Fast Real-Time PCR System (Applied Biosystems, Darmstadt, Germany), and relative transcription levels were determined using β-actin (*Actb*) or glyceraldehyde-3-phosphate dehydrogenase (*Gapdh*) as housekeepers. Deploying PrimerBLAST-Software (National Institutes of Health, Bethesda, MD), primer sequences were designed, while TaqMan probes were derived from Thermo Fisher Scientific (primer sequences and TaqMan probe IDs are provided in Supplementary Table 1).[1]

Transmission Electron Microscopy

For electron microscopy, tissue was fixed at 4°C with 3% glutaraldehyde, washed with PBS, exposed to 2% osmium tetroxide for 30 minutes, dehydrated in series with increasing ethanol concentrations, and embedded in Araldite. Ultrathin (60-nm) sections were cut, mounted on carbon-coated copper grids (Science Service GmbH, Munich, Germany), and contrasted with a saturated solution of uranyl acetate (Merck KGaA, Darmstadt, Germany) in H_2O. The grids were examined with a JEOL 1400 plus transmission electron microscope at 120 kV operating voltage.

Immunohistochemistry and Immunofluorescence

For immunohistochemical or immunofluorescence staining, 5-μm sections of paraffin-embedded ileum Swiss rolls were deparaffinized with xylol substitute (Roth, Karlsruhe, Germany), incubated in citrate buffer for 3 minutes, and subsequently blocked with blocking serum (Vectastain for 5-bromo-2′-deoxyuridine [BrdU]) for 20 minutes. For anti-BrdU staining, mice were pulsed with 10 mg/kg BrdU body weight 1.5 hours before being humanely killed. Primary antibodies used were mouse anti-BrdU (1:10 dilution; BD Biosciences, Heidelberg, Germany), rabbit anti–p-4E-BP1 (1:300 dilution in bovine serum albumin [BSA]; Cell Signaling, Leiden, The Netherlands), goat anti-phosphorylated form of H2A histone family member X (γH2Ax) (1:500 dilution in BSA; Cell Signaling, Leiden, The Netherlands), and goat anti-lysozyme (1:500 dilution in BSA; Santa Cruz Biotechnology, Heidelberg, Germany). Incubation of primary antibodies was performed at 4°C overnight. Sections were washed and incubated with secondary antibodies goat anti-mouse immunoglobulin G for immunohistochemistry (1:1000 in BSA; Jackson ImmunoResearch, Ely, UK) and donkey Alexa Fluor 488 for immunofluorescence (1:500 in BSA; Invitrogen, Darmstadt, Germany), and 3,3′-diaminobenzidine tetra hydrochloride (DAB) substrate (Vectastain ABC Kit, Thermo Fisher Scientific, Steineich, Germany). Stainings were developed with DAB. Slides were counterstained with hematoxylin or 4′,6-diamidino-2-phenylindole and mounted.

For terminal deoxynucleotidyl transferase–mediated deoxyuridine triphosphate nick-end labeling assay, slides were treated with the Apop Tag Plus Peroxidase In Situ Apoptosis Detection Kit (Merck Millipore, Darmstadt, Germany) according to the manufacturer' protocol. Slides were visualized by an AxioImager Z1 microscope (Zeiss, Oberkochen, Germany). Images were captured by a digital camera system (AxioCam HrC/HrM, Zeiss, Oberkochen, Germany). Measurements were made using a semiautomated image analysis software (AxioVision version 08/2013). For the immunohistochemistry analysis, each dot in the accompanying statistical analysis represents 1 individual mouse, for which the mean number of positively stained cells with the respective antibody was assessed in a total of 30 to 50 crypts.

Immunoblot Analysis

Cells were lysed using sodium dodecyl sulfate (SDS)–based direct lysis buffer with 1% Halt Protease inhibitor cocktail (Thermo Fisher Scientific, Darmstadt, Germany), heated at 95°C for 5 minutes, and exposed to ultrasonication for 5 seconds twice. Lysates were centrifuged at 16,000*g* for 15 minutes at 4°C to remove cell remnants. For protein extraction of organoids, Matrigel was removed by several centrifugation steps at 4°C, followed by lysis, as described earlier. Afterward, equal amounts of lysates containing Laemmli buffer were electrophoresed on 12% polyacrylamide gels under standard SDS- polyacrylamide gel electrophoresis conditions before being transferred onto polyvinylidene fluoride membranes (GE Healthcare, Hamburg, Germany). Protein-loaded membranes were blocked with 5% milk in Tris-buffered saline and Tween 20 before being incubated with the primary antibody at 4°C overnight, followed by incubation with a horseradish peroxidase–conjugated secondary antibody for 1 hour at indicated concentrations (Supplementary Table 2). Proteins were detected using the Amersham ECL Prime Western Blot Detection Reagent (GE Healthcare, Hamburg, Germany).

Organoid Culture, Colony Formation Assay, and CellTiter-Glo 3D Viability Assay

Intestinal crypts were isolated from healthy tissue of young (8- to 12-week-old) mice and cultured in Matrigel as previously described.[2] As culture medium for the organoids, a conditioned medium containing Wnt3A, R-spondin1, and Noggin was prepared using L-WRN cells (CRL-3276, ATCC) according to the manufacturers' protocols. When crypts were freshly seeded or when organoids were passaged, the 50% L-WRN medium was supplemented with 10 μmol/L Y-27632 (STEMCELL Technologies, Cologne, Germany). For

passaging, Matrigel was dissolved in Cell Recovery Solution (BD Biosciences, Heidelberg, Germany), and organoids were enzymatically dissociated using TrypLE Express (Gibco, Thermo Fisher Scientific, Darmstadt, Germany). To perform colony formation or CellTiter-Glo assays, organoids were dispersed into single cell solutions using TrypLE Express (Thermo Fisher Scientific, Darmstadt, Germany). For colony formation assays, 10,000 cells per organoid genotype were reseeded onto 24-well plates to assess proliferative capacities by determining both organoid diameters and numbers. For CellTiter-Glo assays, 1500 single cells were replated onto 96-well plates before after 24 hours, CellTiter-Glo 3D reagent (Promega, Mannheim, Germany) was added to each well in 1:1 ratio, and mixtures were homogenized by vigorous pipetting. Plates were then incubated at room temperature for 30 minutes in the dark, with gentle shaking, and luminescence was recorded using an automatic plate reader (CLARIOstar, BMG Labtech, Ortenberg, Germany). Images were acquired using the Leica M205FCA microscope equipped with a Leica DFC9000 GT camera and the Leica LAS X software (Wetzlar, Germany) (4× magnification). For rescue experiments, organoids in both assays were treated with dimethyl sulfoxide or 1 μmol/L rapamycin (LC Laboratories, Hamburg, Germany) dissolved in dimethyl sulfoxide.

Murine Intestinal Epithelial ModeK Cells, 3-(4,5-Dimethylthiazol-2-yl)-5-(3-Carboxymethoxyphenyl)-2-(4-Sulfophenyl)-2H-Tetrazolium Assay

i*Xbp1* ModeK cells were generated by transfection of the respective cells with plasmids that intracellularly were transcribed into Xbp1-intering RNA sequences.[2] Knockdown was validated by quantitative PCR analysis. For immortalization, we used the SV40 Virus (simian vacuolating virus). Cells were cultivated at 37°C with Dulbecco's modified Eagle medium GlutaMAX medium (Gibco, Darmstadt, Germany) with 10% fetal calf serum (Merck Millipore, Darmstadt, Germany). Medium was exchanged every other day. Viability of ModeK cells cultivated on 96-well plates was assessed by measuring 3-(4,5-dimethylthiazol-2-yl)-5-(3-carboxymethoxyphenyl)-2-(4-sulfophenyl)-2H-tetrazolium (MTS) incorporation using the CellTiter 96 AQueous One Solution Cell Proliferation Assay (Promega, Mannheim, Germany) according to the manufacturer's protocol.

Fluorescence-Activated Cell Sorter Annexin Cell Death Assay

ModeK cells and organoids of the respective genotypes were seeded onto 24-well plates. For fluorescence-activated cell sorter (FACS)–based cell death assay using Annexin V-FITC (ImmunoTools, Friesoythe, Germany) and 7-aminoactinomycin (7-AAD; BD Biosciences), cells were dissociated using TrypLE Express (Thermo Fisher Scientific, Darmstadt, Germany). Cells were then incubated in Annexin V and 7-AAD before FACS assay was performed using FACSCalibur (BD Biosciences, Heidelberg, Germany). Then, 10,000 cells were gated, excluding doublets or non-dissociated cell groups. The fraction of cells positive for annexin staining was considered as dead cells.

Transfection of ModeK Cells With Small Interfering RNA

For in vitro transfection, Viromer Blue (Lipocalyx, Halle, Germany) was used according to the manufacturers' protocol. Small interfering RNA against *Ddit4l* (#GS73284) and *p53* (#GS22059) was derived from Qiagen (Hilden, Germany) and used at a concentration of 10 μmol/L.

Stimulants for ModeK Cells and Organoids

As stimulants for ModeK cells and organoids, AraC (received as a gift from a collaborator at the Institute of Biochemistry, CAU Kiel), IWP-2 (tebu-bio, Offenbach, Germany), and rapamycin (LC Laboratories, Hamburg, Germany) were used.

In Silico RNA Sequencing Data Analysis

RNA sequencing expression profiles and clinical data for colorectal cancer (COAD—Colon Adenocarcinoma and READ—Rectum Adenocarcinoma) were downloaded from TCGA (http://gdac.broadinstitute.org/). Only samples from primary tumors, for which clinical survival data was available, were considered in the analysis (n = 376). RNA sequencing expression data were transformed to $\log_2$ (transcripts-per-millions +1).

Survival Analysis

Overall survival analysis was performed using the R package survival (The R Foundation for Statistical Computing, Vienna, Austria). Samples were divided into 2 groups based on their *XBP1* gene expression ("*XBP1* high" and "*XBP1* low") by using the maximum Harrell's C-index. The Cox's proportional hazards model was used to evaluate the association between *XBP1* gene expression and the survival time of the patients. Kaplan-Meier survival curves with log-rank tests were plotted to compare the overall survival between the 2 groups. Additionally, the hazard ratio (HR) with a 95% CI was provided for comparison of the groups. *P* values were adjusted for multiple testing based on their false discovery rate according to the Benjamini-Hochberg procedure.

Pathway Activity Analysis

Pathway activity scores for 14 cancer-related pathways (androgen, estrogen, WNT, epidermal growth factor receptor, mitogen-activated protein kinase, phosphoinositide 3-kinase, vascular endothelial growth factor, Janus kinase-signal transducer of activation , transforming growth factor-β, tumor necrosis factor-α, nuclear factor-κB, hypoxia, tumor necrosis factor-related apoptosis-inducing ligand, and p53-mediated DDR were estimated using Pathway RespOnsive GENes (PROGENy). This method embarks on a compendium of pathway-responsive gene signatures derived from perturbation experiments to infer pathway activity. To prepare the gene expression data for PROGENy,[3] raw count data were imported to the R package DESeq2. Additionally, a linear model was applied to check for differences between the 2 groups ("*XBP1* high" and "*XBP1* low").

Supplementary References

1. Aden K, Bartsch K, Dahl J, et al. Epithelial RNase H2 maintains genome integrity and prevents intestinal tumorigenesis in mice. Gastroenterology 2019; 156:145–159.e19.
2. Aden K, Breuer A, Rehman A, et al. Classic IL-6R signalling is dispensable for intestinal epithelial proliferation and repair. Oncogenesis 2016;5. e270–e270.
3. Schubert M, Klinger B, Klünemann M, et al. Perturbation-response genes reveal signaling footprints in cancer gene expression. Nat Commun 2018;9:20.

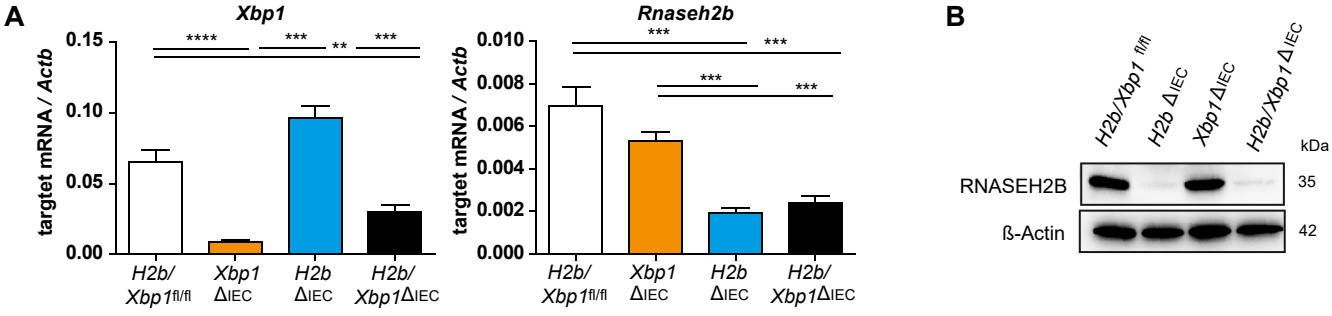

Supplementary Figure 1. Validation of conditional knockout. Validation of successful *Rnaseh2b* and *Xbp1* knockout in small intestinal *H2b/Xbp1*$^{fl/fl}$, *Xbp1*$^{\Delta IEC}$, *H2b*$^{\Delta IEC}$, and *H2b/Xbp1*$^{\Delta IEC}$ organoids, representative of a minimum of 3 individual experiments. (*A*) Quantitative polymerase chain reaction analysis with 3 technical replicates. Relative messenger RNA (mRNA) expression is normalized to β-actin (*Actb*). Data are expressed as mean ± standard error of the mean, and significance was determined using an unpaired Student *t* test. $^{**}P < .01$; $^{***}P < .0001$; $^{****}P < .00001$. (*B*) Knockout of *Rnaseh2b* was additionally validated on the protein level. β-Actin served as a loading control.

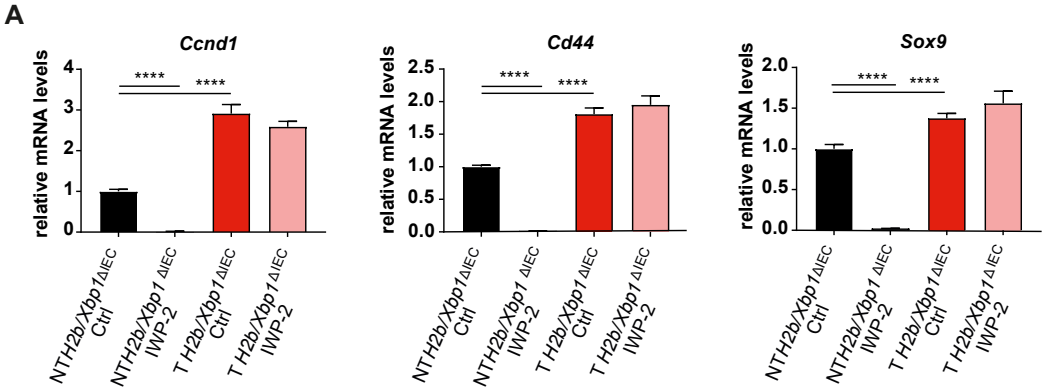

Supplementary Figure 2. *H2b/Xbp1*$^{\Delta IEC}$ tumor organoids exhibit autonomous Wnt pathway activation. Quantitative reverse-transcription analysis of nontumor (NT) or tumor (T) *H2b/Xbp1*$^{\Delta IEC}$ organoids, unstimulated or treated with 2 μmol/L of the Wnt inhibitor IWP-2 for 72 hours, representative of a minimum of 3 individual experiments with 3 technical replicates. Ctrl, control. Expression levels are displayed as relative messenger RNA (mRNA) levels. Data are expressed as mean ± standard error of the mean, and significance was determined using an unpaired Student *t* test. ****$P < .00001$.

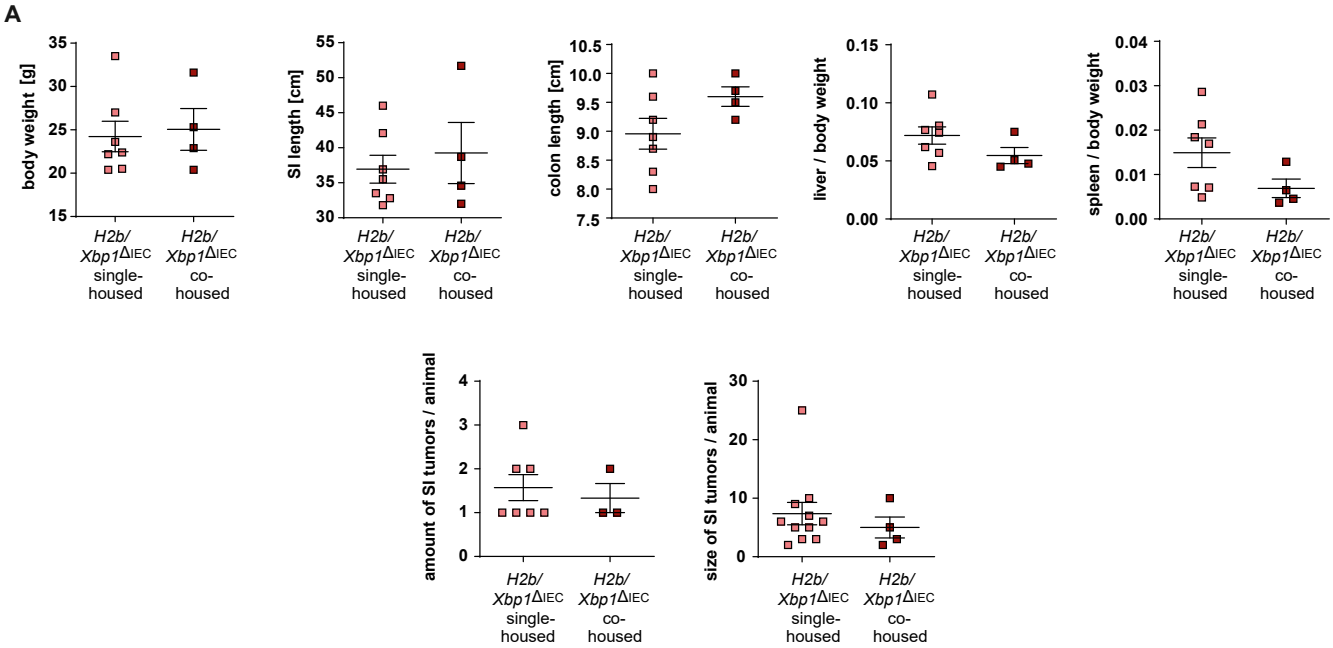

Supplementary Figure 3. Comparison of clinical phenotype of single-housed vs cohoused aged *H2b/Xbp1*$^{\Delta IEC}$ mice. Basal phenotyping analysis of 52-week-old single-housed (n = 7; 6 females, 1 male) vs cohoused (n = 4; 3 females, 1 male) *H2b/Xbp1*$^{\Delta IEC}$ mice, consisting of body weight, small intestine (SI) length, colon length, liver weight, and spleen weight in correlation to body weight, and amount and size of SI tumors per animal. Each dot represents 1 individual. In cohousing conditions, *H2b/Xbp1*$^{\Delta IEC}$ and *H2b/Xbp1*$^{fl/fl}$ mice were kept in a 1:1 ratio. Data are expressed as mean ± standard error of the mean ,and significance was determined using an unpaired Student *t* test.

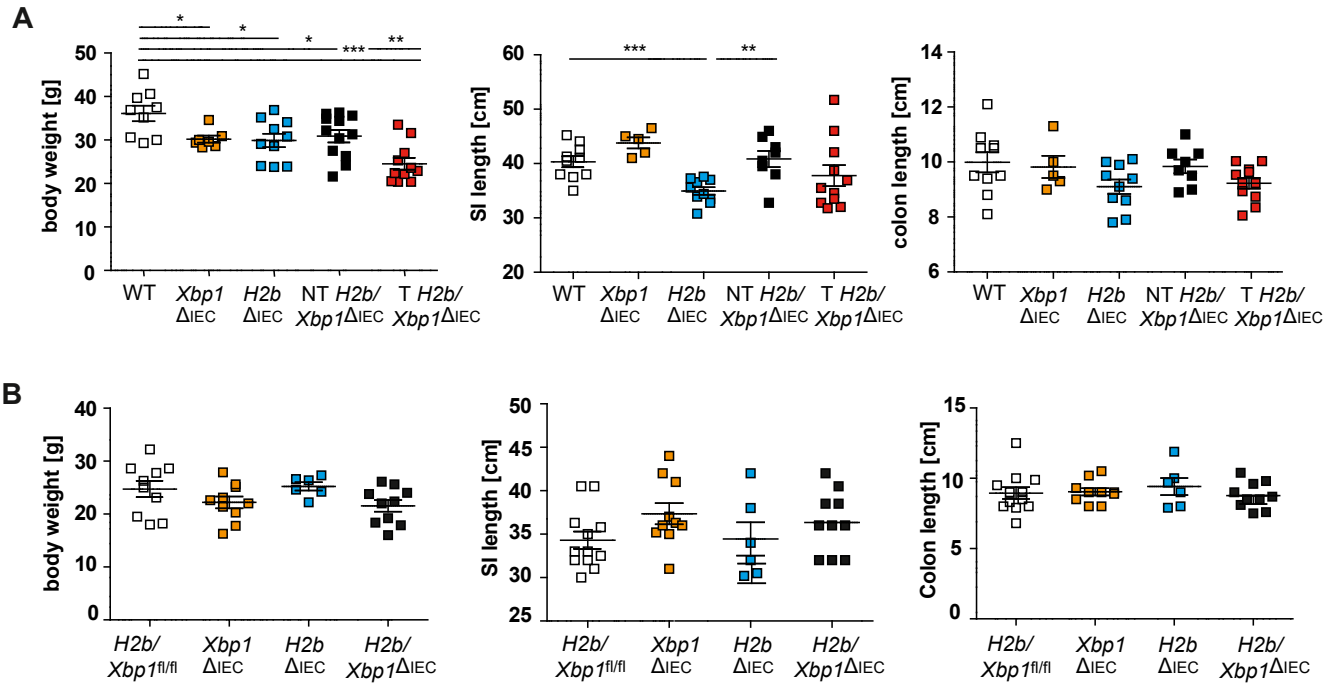

Supplementary Figure 4. Clinical phenotype in aged *H2b/Xbp1*$^{\Delta IEC}$ mice. (*A*) Basal phenotyping analysis of 52-week-old wild-type (WT) (n = 10, 10 males), *Xbp1*$^{\Delta IEC}$ (n = 7; 1 female, 6 males), *H2b*$^{\Delta IEC}$ (n = 10; 4 females, 6 males), and nontumor (NT) and tumor (T) *H2b/Xbp1*$^{\Delta IEC}$ (n = 21; 12 females, 9 males) mice. (*B*) Basal phenotyping analysis of 8- to 12-week old WT (n = 10, 10 males), *Xbp1*$^{\Delta IEC}$ (n = 7; 1 female, 6 males), *H2b*$^{\Delta IEC}$ (n = 10; 4 females, 6 males), and *H2b/Xbp1*$^{\Delta IEC}$ (n = 21; 12 females, 9 males) mice. Analysis parameters include body weight, small intestine (SI) length, and colon length. Each dot represents 1 individual. Data are expressed as mean ± standard error of the mean, and significance was determined using an unpaired Student *t* test. **P* < .05; ***P* < .01; ****P* < .0001.

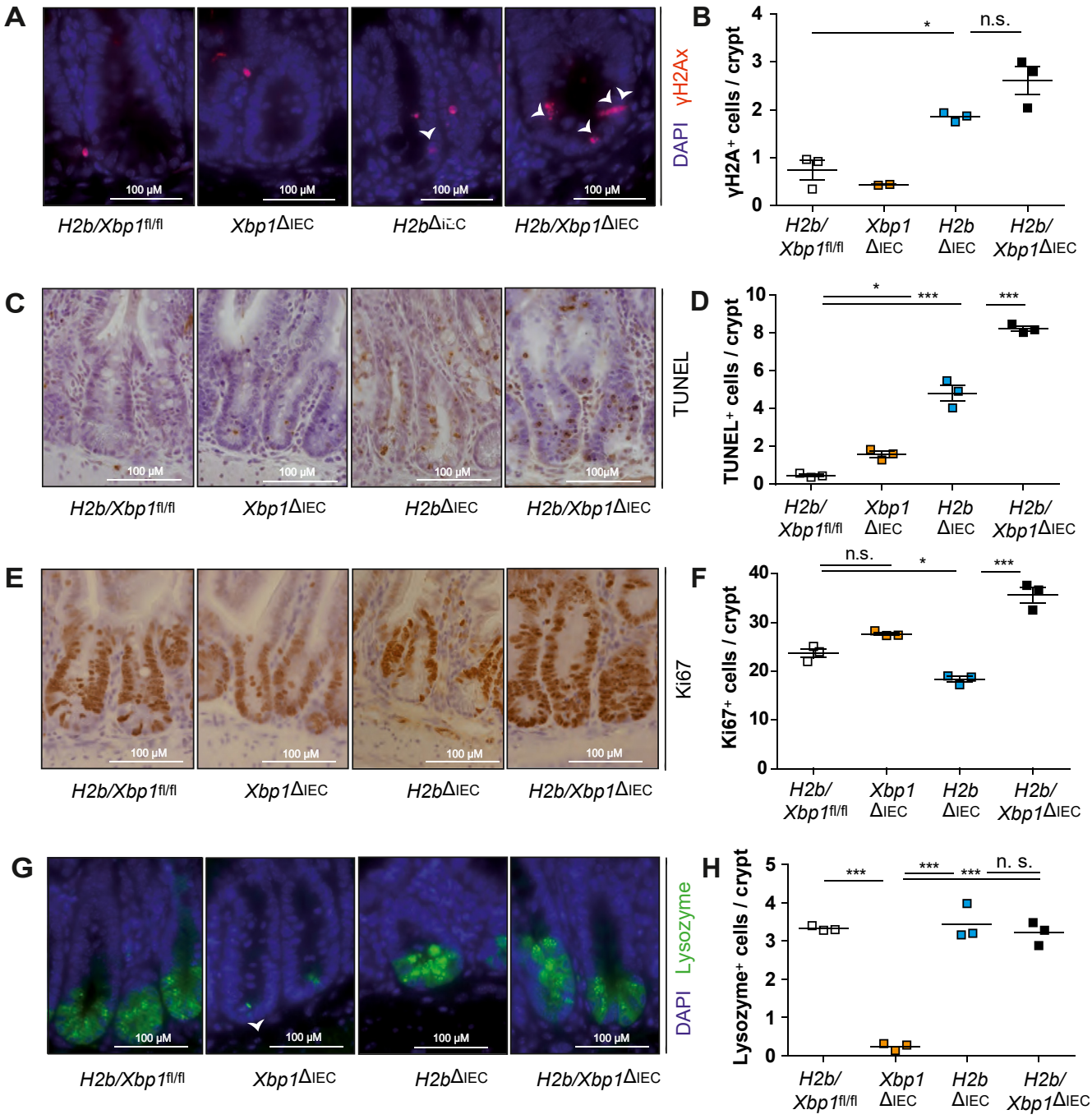

Supplementary Figure 5. *Xbp1* deficiency limits intestinal epithelial regeneration in 8- to 12- week old mice. Representative images of the small intestine (SI) of 8- to 12-week-old *H2b/Xbp1*$^{fl/fl}$ (n = 3; 1 female, 2 males), *Xbp1*$^{\Delta IEC}$ (n = 2; 1 female, 1 male), *H2b*$^{\Delta IEC}$ (n = 3; 2 females, 1 male), and *H2b/Xbp1*$^{\Delta IEC}$ (n = 3; 1 female, 2 males) mice, stained for (*A*) the phosphorylated form of H2A histone family member X (γH2Ax), with *white arrowheads* indicating γH2Ax^{+} nuclei, (*C*) terminal deoxynucleotidyl transferase–mediated deoxyuridine triphosphate nick-end labeling (TUNEL), (*E*) Ki67, and (*G*) lysozyme. DAPI, 4′,6-diamidino-2-phenylindole. Each *dot* in the accompanying statistical analyses represents 1 individual, for which the mean number of (*B*) γH2Ax^{+}, (*D*) TUNEL^{+}, (*F*) Ki67^{+}, and (H) lysozyme^{+} cells was assessed in a total of 50 crypts. Data are expressed as mean ± standard error of the mean, and significance was determined using 1-way analysis of variance. n.s., not significant; **P* < .05, ****P* < .001.

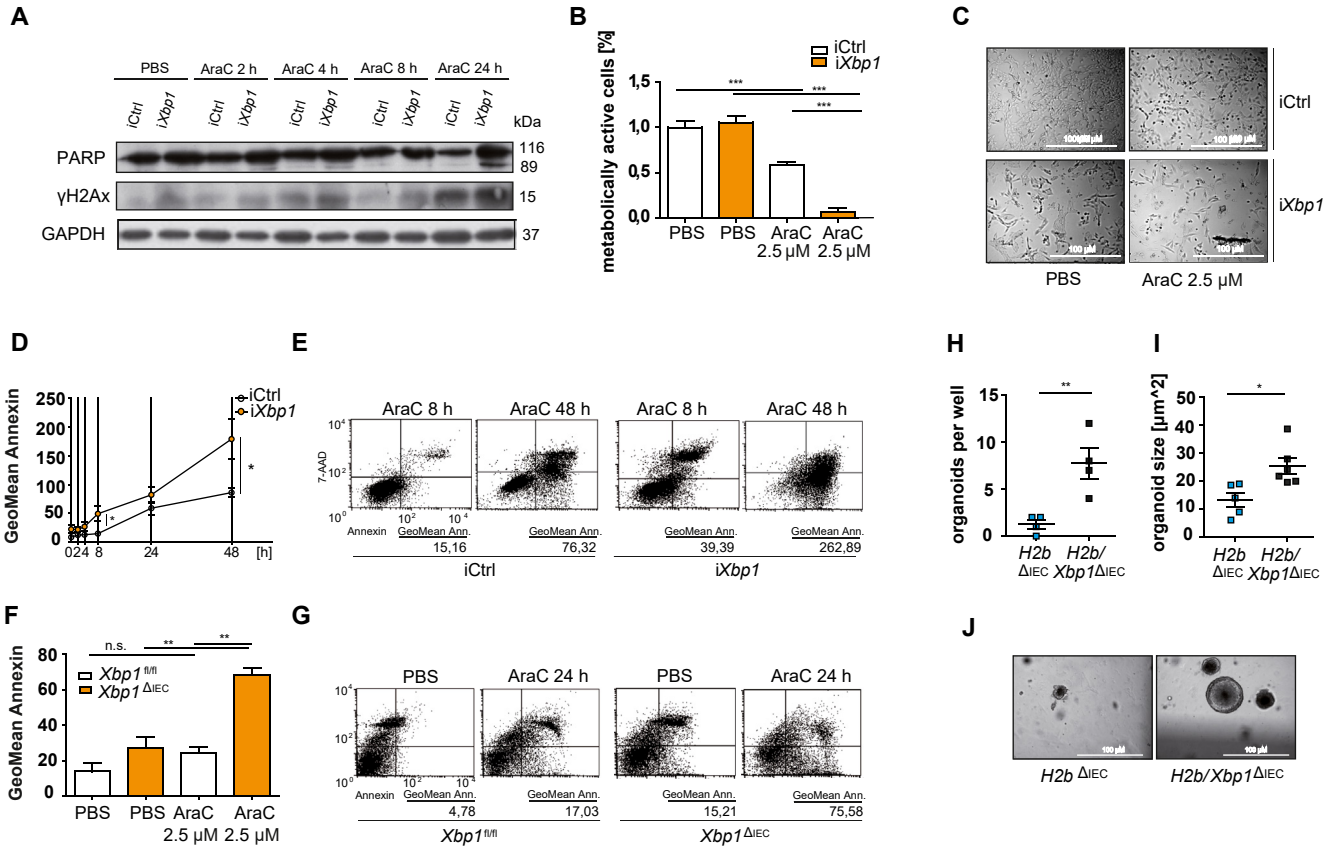

Supplementary Figure 6. *Xbp1* deficiency limits intestinal epithelial regeneration in the context of DNA damage in vitro. (*A*) Western blot of the phosphorylated form of H2A histone family member X (γH2Ax) and poly (adenosine diphosphate-ribose) polymerase (PARP) of ModeK cells, treated with 2.5 μmol/L AraC for 2, 4, 8, and 24 hours, representative of a minimum of 3 individual experiments with 3 technical replicates. Glyceraldehyde-3-phosphate dehydrogenase (GAPDH) served as a loading control. (*B*) MTS (3-(4,5-dimethylthiazol-2-yl)-5-(3-carboxymethoxyphenyl)-2-(4-sulfophenyl)-2H-tetrazolium) assay of ModeK cells, representative of a minimum of 3 individual experiments with 5 technical replicates, treated with phosphate-buffered saline (PBS) or 2.5 μmol/L AraC for 24 hours. After medium exchange, cells recovered for 48 hours. (*C*) Representative images of ModeK cells stimulated with PBS or 2.5 μmol/L AraC for 24 hours (scale bar = 100 μM). (*D*) Fluorescence-activated cell sorting (FACS) annexin (Ann.) assay of ModeK cells, representative of a minimum of 3 individual experiments with 3 technical replicates, treated with 2.5 μmol/L AraC for 0, 2, 4, 8, 24, and 48 hours, with (*E*) corresponding *dot plots* at 8 and 48 hours. (*F*) FACS annexin assay of *Xbp1*$^{fl/fl}$ or *Xbp1*$^{\Delta IEC}$ intestinal organoids, representative of a minimum of 3 individual experiments with 3 technical replicates, stimulated with PBS or 2.5 μmol/L AraC for 24 hours, with (*G*) corresponding *dot plots*. Colony forming assay of untreated intestinal organoids of the indicated genotypes, demonstrating the (*H*) amount or (*I*) diameter of regrown organoids on day 10 after reseeding, with (*J*) representative images (scale bar = 100 μM). Data are expressed as mean ± standard error of the mean, and significance was determined using an unpaired Student *t* test. n.s., not significant; *$P < .05$, **$P < .01$, ***$P < .0001$.

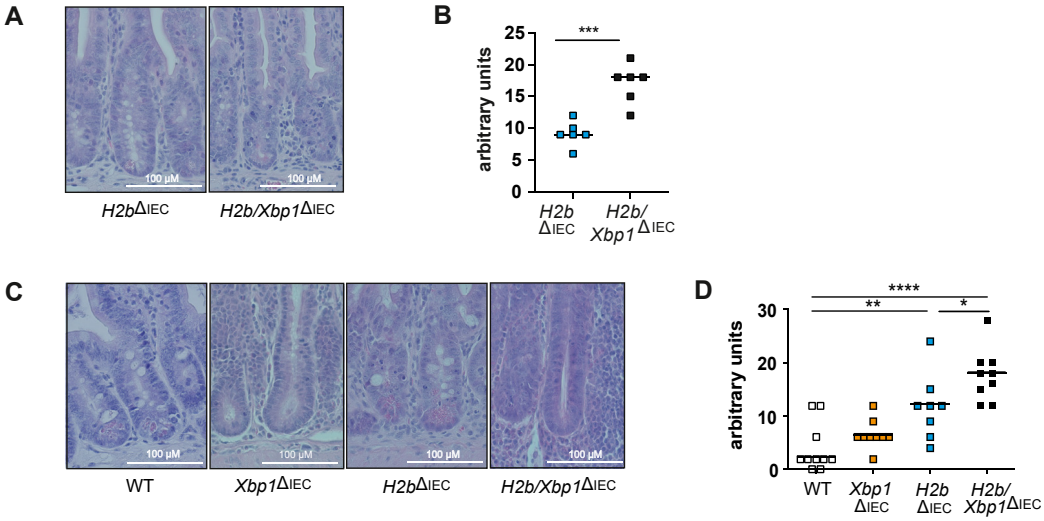

Supplementary Figure 7. Deletion of *Xbp1* drives mucosal inflammation upon DSS-induced colitis. Representative H&E images of small intestines (SI) of mice with the respective genotypes being opposed to (*A*) acute and (*C*) chronic DSS-induced colitis, with (*B*, *D*) corresponding histopathologic scoring of the SI; each *dot* represents the histopathologic score of 1 individual mouse. For histopathologic evaluation of chronic DSS colitis, 2 independent chronic DSS-induced colitis models were individually analyzed before data were pooled for final assessment. WT, wild-type. Data are expressed as mean ± standard error of the mean, and significance was determined using an unpaired Student *t* test. $^{*}P < .05$, $^{**}P < .01$, $^{****}P < .00001$.

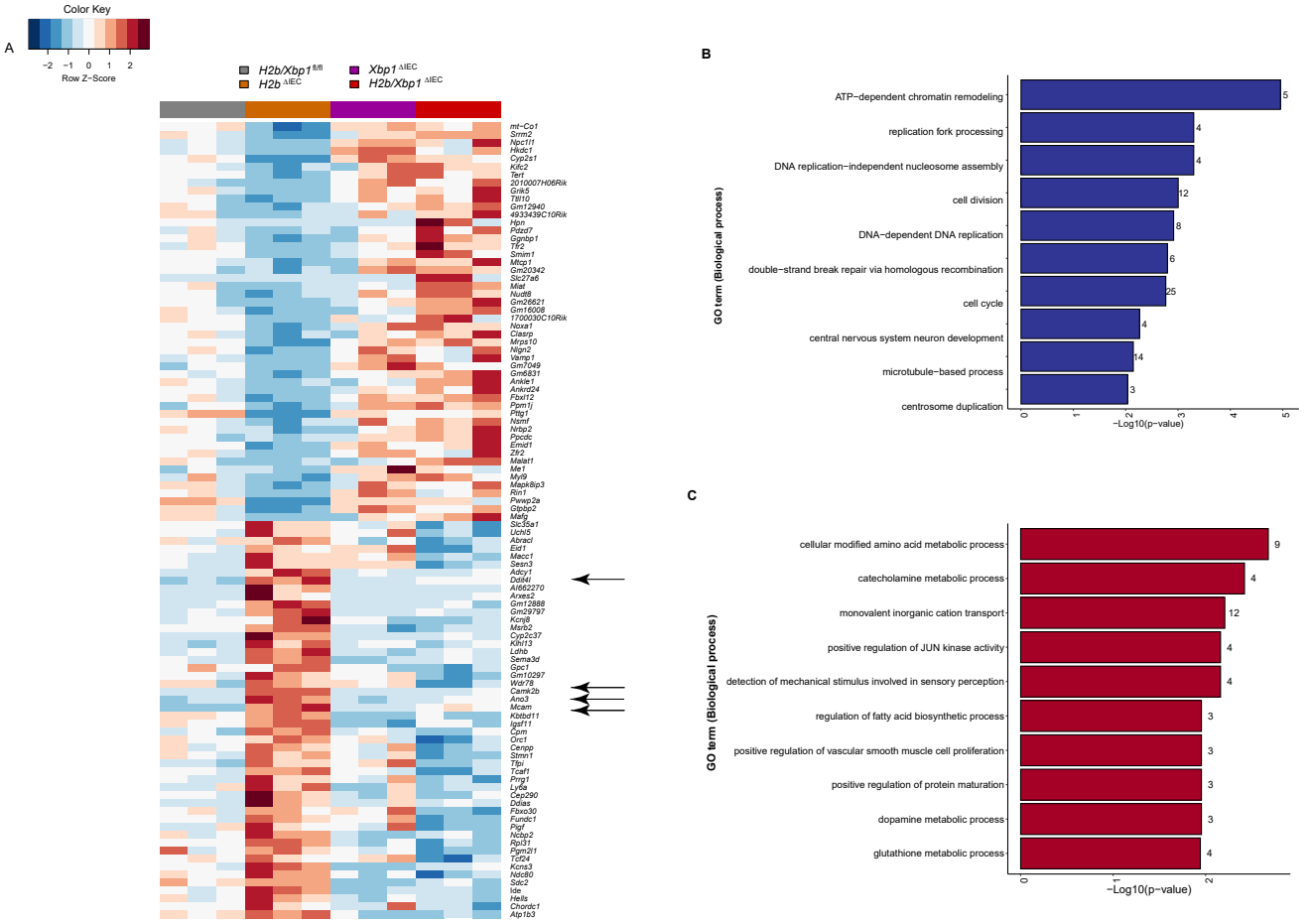

Supplementary Figure 8. *H2b/Xbp1*$^{\Delta IEC}$ mice display a distinct transcriptional signature. (*A*) Top differential gene expression between *H2b*$^{\Delta IEC}$ vs *H2b/Xbp1*$^{\Delta IEC}$ compared with *H2b/Xbp1*$^{fl/fl}$ organoids. (*B*) Top 10 Gene Ontology (GO) biological processes in genes downregulated and (*C*) upregulated in *H2b*$^{\Delta IEC}$ vs *H2b/Xbp1*$^{\Delta IEC}$ organoids but not in *H2b/Xbp1*$^{fl/fl}$ vs *H2b/Xbp1*$^{\Delta IEC}$. ATP, adenosine 5′-triphosphate.

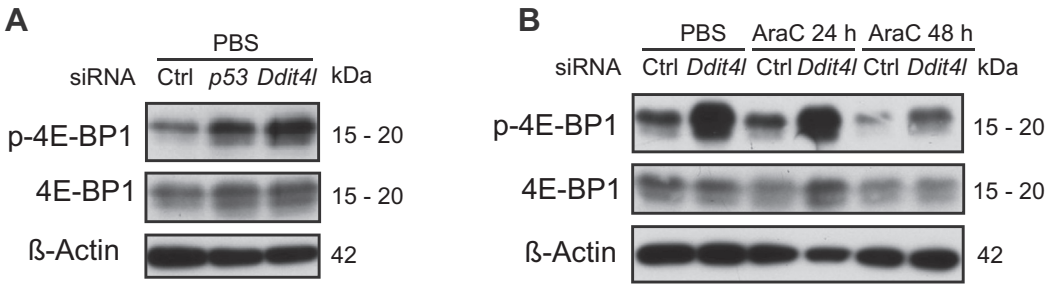

Supplementary Figure 9. DDIT4L regulates endogenous 4E-BP1 phosphorylation in IECs. (*A*) iCtrl ModeK cells were transfected with small interfering (si)RNA against Ddit4l and p53 for 24 hours, and protein lysates were probed against p-4E-BP1. β-Actin was used as loading control. Representative image of a minimum of 3 individual experiments. PBS, phosphate buffered saline. (*B*) iCtrl ModeK cells were transfected with siRNA against Ddit4l and stimulated with 2.5 μmol/L AraC for 24 or 48 hours. Protein lysates were probed against p-4E-BP1. β-Actin was used as loading control. Representative image of minimum of 3 individual experiments.

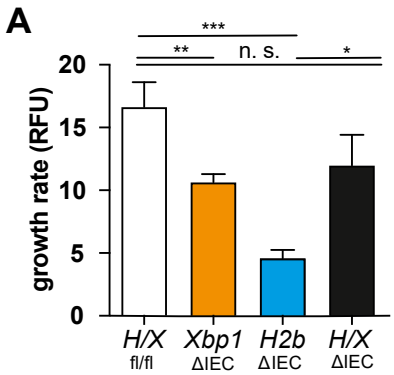

Supplementary Figure 10. Deficiency of *Xbp1* restores proliferation in *H2b*$^{\Delta IEC}$ organoids. CellTiter-Glo assay of untreated intestinal *H2b/Xbp1*$^{fl/fl}$, *Xbp1*$^{\Delta IEC}$, *H2b*$^{\Delta IEC}$, and *H2b/Xbp1*$^{\Delta IEC}$ organoids after a growing period of 72 hours. Representative data of 3 individual experiments with 3 technical replicates. *H2b/Xbp1*$^{fl/fl/\Delta IEC}$ organoids are abbreviated as "*H/X*$^{fl/fl/\Delta IEC}$." RFU, relative fluorescent units. Data are expressed as mean ± standard error of the mean, and significance was determined using an unpaired Student *t* test. n.s., not significant; *$P < .05$, **$P < .01$, ***$P < .0001$.

Supplementary Table 1. TaqMan and SYBR Green Probes and Primers

Gene name	Forward sequence (5′ and 3′) SYBR green	Backward sequence (5′ and 3′) SYBR green
Actb	GATCGGTGGCTCCATCCTGGC	CGCAGCTCAGTAACAGTCCGCC
Gapdh	CCGGGGCTGGCATTGCTCTCA	CTTGCTCAGTGTCCTTGCTGGGG
p53	CTAGCATTCAGGCCCTCATC	TCCGACTGTGACTCCTCCAT
Xbp1	TGGCCGGGTCTGCTGAGT	ACAGGGTCCAACTTGTCCAG

Gene name	Species	TaqMan probe ID
Actb	Murine	00607939
Ccnd1	Murine	00432359
Ccng1	Murine	00438084
Cd44	Murine	01277161
Ddit4l	Murine	00513313
Mdm2	Murine	01233138
Rnaseh2b	Murine	01317628
Sesn2	Murine	00460679
Sox9	Murine	00448840

Supplementary Table 2. Antibodies Used for Western Blot Analysis

Western blot antibody	Origin	Dilution	Company	Article number
Primary				
β-Actin	Mouse	1:1000 in 5% BSA in TTBS	Sigma-Aldrich	A-5441
β-Tubulin	Rabbit	1:1000 in 5% BSA in TTBS	Abcam	ab6046
GAPDH	Mouse	1:1000 in 5% BSA in TTBS	Santa Cruz Biotechnology	sc-365062
PARP	Rabbit	1:1000 in 5% BSA in TTBS	Cell Signaling Technology	9542
p53	Mouse	1:1000 in 5% BSA in TTBS	Cell Signaling Technology	2524T
pS6	Rabbit	1:1000 in 5% BSA in TTBS	Cell Signaling Technology	5364
p-4E-BP1	Rabbit	1:2000 in 5% BSA in TTBS	Cell Signaling Technology	2855
RNASEH2B	Rabbit	1:2000 in 5% BSA in TTBS	Received from collaborator[1]	-
S6	Rabbit	1:1000 in 5% BSA in TTBS	Cell Signaling Technology	2317
yH2Ax	Rabbit	1:1000 in 5% BSA in TTBS	Cell Signaling Technology	2577
4E-BP1	Rabbit	1:2000 in 5% BSA in TTBS	Cell Signaling Technology	9644
Secondary				
Rabbit IgG, HRP-linked	Sheep	1:3000 in 5% BSA in TTBS	GE Healthcare	NA934-1ML
Mouse IgG, HRP-linked	Sheep	1:3000 in 5% BSA in TTBS	GE Healthcare	NA931-1ML

BSA, bovine serum albumin; GAPDH, glyceraldehyde-3-phosphate dehydrogenase; Ig, immunoglobulin; HRP, horseradish peroxidase; PARP, poly (adenosine diphosphate-ribose) polymerase; TTBS, Tween-Tris–buffered saline.